Spheroid's Panchromatic Investigation in Different Environmental Regions (SPIDER) – I. Sample and galaxy parameters in the griz$YJHK$ wavebands.

F. La Barbera[1]⋆, R.R. de Carvalho[2], I.G. de la Rosa[3], P.A.A. Lopes[4],
J.L.Kohl-Moreira[5] and H.V. Capelato[2]

[1]*INAF – Osservatorio Astronomico di Capodimonte, Napoli, Italy*
[2]*Instituto Nacional de Pesquisas Espaciais/MCT, S. J. dos Campos, Brazil*
[3]*Instituto de Astrofísica de Canarias, Tenerife, Spain*
[4]*Observatório do Valongo/UFRJ, Rio de Janeiro, Brazil*
[5]*Observatório Nacional/MCT, Rio de Janeiro, Brazil*

ABSTRACT

This is the first paper of a series presenting a Spheroid's Panchromatic Investigation in Different Environmental Regions (SPIDER). The sample of spheroids consists of 5,080 bright ($M_r < -20$) Early-Type galaxies (ETGs), in the redshift range of 0.05 to 0.095, with optical (griz) photometry and spectroscopy from SDSS-DR6 and Near-Infrared (YJHK) photometry from UKIDSS-LAS (DR4). We describe how homogeneous photometric parameters (galaxy colors and structural parameters) are derived using $grizYJHK$ wavebands. We find no systematic steepening of the CM relation when probing the baseline from g-r to g-K, implying that internal color gradients drive most of the mass-metallicity relation in ETGs. As far as structural parameters are concerned we find that the mean effective radius of ETGs smoothly decreases, by 30%, from g through K, while no significant dependence on waveband is detected for the axis ratio, Sersic index, and a$_4$ parameters. Also, velocity dispersions are re-measured for all the ETGs using STARLIGHT and compared to those obtained by SDSS. The velocity dispersions are re-derived using a combination of simple stellar population models as templates, hence accounting for the kinematics of different galaxy stellar components. We compare our (2DPHOT) measurements of total magnitude, effective radius, and mean surface brightness with those obtained as part of the SDSS pipeline (Photo). Significant differences are found and reported, including comparisons with a third and independent part. A full characterization of the sample completeness in all wavebands is presented, establishing the limits of application of the characteristic parameters presented here for the analysis of the global scaling relations of ETGs.

Key words: galaxies: fundamental parameters – formation – evolution

1 INTRODUCTION

We have witnessed tremendous advances in our ability to measure galaxy properties with unprecedented accuracy over the past two decades. The greatest leap forward was the advent of the CCD, with an order of magnitude increase in sensitivity over photographic film and the ability to easily make quantitative measurements. Today, surveys like the Sloan Digital Sky Survey (SDSS) and UKIRT Infrared Deep Sky Survey (UKIDSS) provide access to high quality data covering a large wavelength range, probing different astro-

physical aspects of the galaxies. These advances have been immediately applied to examining the global properties of galaxies.

Understanding the formation and evolution of galaxies requires probing them over a long time (redshift) baseline to establish the physical processes responsible for their current observed properties. It is far easier to measure nearby ETGs as opposed to their counterparts at high redshift, and this must be borne in mind when comparing samples at opposite distance extremes. Almost as soon as high quality data became available for nearby samples of ETGs it was recognized that they occupy a 2-dimensional space, the fundamental plane (FP), represented by the quantities radius, velocity dispersion, and surface brightness R - σ - μ. Brosche (1973) was the first to examine ETGs using multi-variate statistical techniques, applying Principal Component Analysis (PCA) to the relatively poor

data available. Although his results were not fully appreciated at the time, it drew the attention of other researchers who further studied the implications of the FP (Djorgovski 1987; Dressler et al. 1987). Brosche's fundamental contribution was to show that we should be looking for sets of data with the smallest number of significant principal components when starting from a large number of input parameters. In this way we reduce a high-dimensional dataset to only those quantities that are likely to have physical meaning. Several studies followed Brosche's: Bujarrabal, Guibert & Balkowski (1981), Efstathiou & Fall (1984), Whitmore (1984), and Okamura et al. (1984).

The fundamental plane is a bivariate scaling law between R, σ, and I, where μ = -2.5 log I, expressed as R $\sim \sigma^A I^B$. In order to obtain accurate and meaningful coefficients that can be compared to theoretical expectations (such as those from the Virial Theorem, which implies A = 2 and B= -1) we need to not only have a homogeneous sample of ETGs, but also to understand the selection effects in defining the sample and to properly measure the photometric and spectroscopic quantities involved. Several contributions in the past have met most of these requirements (Graham & Colless 1997; Jørgensen et al. 1996). However, the lack of homogeneous data covering a large wavelength baseline while also probing the entire range of environments (local galaxy density) impeded further progress. Bernardi et al. (2003a,b), Bernardi et al. (2006), and Bernardi et al. (2007) were the first to fill this gap and set strong constraints on the FP coefficients and their implications, though limited to the optical regime (see also Hyde & Bernardi 2009). Another important and often overlooked aspect of such studies is the impact of different techniques and implementations for measuring R - σ - μ and their respective errors, which ultimately will be propagated and compared to the distribution of residuals around the FP (Prugniel & Simien 1996; Gargiulo et al. 2009).

This is the first paper of a series presenting the Spheroid's Panchromatic Investigation in Different Environmental Regions (SPIDER) survey. SPIDER utilizes optical and Near-Infrared (NIR) photometry in the $grizYJHK$ wavebands as well as spectroscopic data. Spectroscopy and optical photometry are taken from SDSS DR6, while the $YJHK$ data are obtained from the UKIDSS-LAS DR4. In the present work (Paper I), we describe how the sample of ETGs is selected, how the photometric and spectroscopic parameters are derived for each galaxy, and derive an accurate estimate of the completeness of the sample in each band. The $grizYJHK$ galaxy images have been homogeneously analyzed using 2DPHOT, an automatic software designed to obtain both integrated and surface photometry of galaxies in wide-field images (La Barbera et al. 2008a). We present a detailed comparison of the 2DPHOT output quantities (magnitudes and structural parameters) to those provided by the SDSS Photo pipeline (Stoughton et al. 2002). We have also re-computed central velocity dispersions from the SDSS spectra using the software STARLIGHT (Cid Fernandes et al. 2005), and compared these new estimates to those from SDSS. Velocity dispersions are re-derived using a combination of simple stellar population models as templates. This procedure minimizes the well known template mismatch problem, accounting for the different kinematics of various stellar components in a galaxy. All the photometric and spectroscopic measurements presented here are made available through an ascii table at http://www.lac.inpe.br/bravo/arquivos/SPIDER_data_paperI.ascii.[1]

The complete SPIDER data-set is also made available, on request, through a database structure which allows the user to easily retrieve all information by issuing SQL queries.

In Sec. 2, we describe how the galaxy sample is selected. Sec. 3 describes how $grizYJHK$-band images are analyzed to derive integrated photometry and the structural parameters, with corresponding uncertainties. Secs. 4 and 5 compare the overall integrated and structural properties of ETGs from g through K, deriving color–magnitude relations and presenting the distribution of structural parameters in all wavebands. Sec. 6 compares the structural parameters derived from 2DPHOT with those from SDSS. In Sec. 7, we describe the measurement of central velocity dispersions, comparing them to those from SDSS. The completeness of the sample is studied in Sec. 8. A summary is provided in Sec. 9.

Throughout the paper, we adopt a cosmology with $H_0 = 75 \, \mathrm{km \, s^{-1} \, Mpc^{-1}}$, $\Omega_m = 0.3$, and $\Omega_\Lambda = 0.7$.

2   SAMPLE SELECTION

2.1   Sample Definition

The sample of ETGs is selected from SDSS-DR6, following a procedure described in La Barbera et al. (2008b) and La Barbera & de Carvalho (2009), selecting galaxies in the redshift range of 0.05 to 0.095, with $^{0.1}M_r < -20$, where $^{0.1}M_r$ is the k-corrected SDSS Petrosian magnitude in r-band. The k-correction is estimated using the software $kcorrect$ (version 4_1_4; Blanton et al. 2003a, hereafter BL03), through a restframe r-band filter blue-shifted by a factor $(1 + z_0)$ (see also Sec. 3.1). As in previous works (e.g. Hogg et al. 2004), we adopt $z_0 = 0.1$. The lower redshift limit of the sample is chosen to minimize the aperture bias (Gómez et al. 2003), while the upper redshift limit guarantees (1) a high level of completeness (according to Sorrentino et al. 2006) and (2) allows us to define a volume-limited sample of *bright* early-type systems. In fact, ETGs follow two different trends in the size–luminosity diagram (Capaccioli, Caon & D'Onofrio 1992; Graham & Guzmán 2003). The separation between the two families of *bright* and *ordinary* ellipticals occurs at an absolute B-band magnitude of -19, corresponding to the magnitude limit of $M_r \sim -20$ we adopt here. At the upper redshift limit of $z = 0.095$, the magnitude cut of -20 also corresponds approximately to the magnitude limit where the SDSS spectroscopy is complete (i.e. a Petrosian magnitude of $m_r \sim 17.8$). Following Bernardi et al. (2003a), we define ETGs using the SDSS spectroscopic parameter $eClass$, that indicates the spectral type of a galaxy on the basis of a principal component analysis, and the SDSS photometric parameter $fracDev_r$, which measures the fraction of galaxy light that is better fitted by a de Vaucouleurs (rather than an exponential) law. In this contribution, ETGs are those systems with $eClass < 0$ and $fracDev_r > 0.8$. We select only galaxies with central velocity dispersion, σ_0, available from SDSS-DR6, in the range of 70 and $420 \, \mathrm{km \, s^{-1}}$, and with no spectroscopic warning on (i.e. $zWarning$ attribute set to zero). These constrains imply retrieving only reliable velocity dispersion measurements from SDSS. All the above criteria lead to a sample of $39,993$ ETGs.

The sample of ETGs with optical data is then matched to the fourth data release (DR4) of UKIDSS–Large Area Survey (LAS). UKIDSS–LAS DR4 provides NIR photometry in the $YJHK$ bands over ~ 1000 square degrees on the sky, with significant overlap with SDSS (Lawrence et al. 2007). The YHK-band data have a pixel scale of $0.4''/pixel$, matching almost exactly the resolution of the SDSS frames ($0.396''/pixel$). J band observations are

---

[1] The file is mirrored at http://www.na.astro.it/ labarber/SPIDER/.
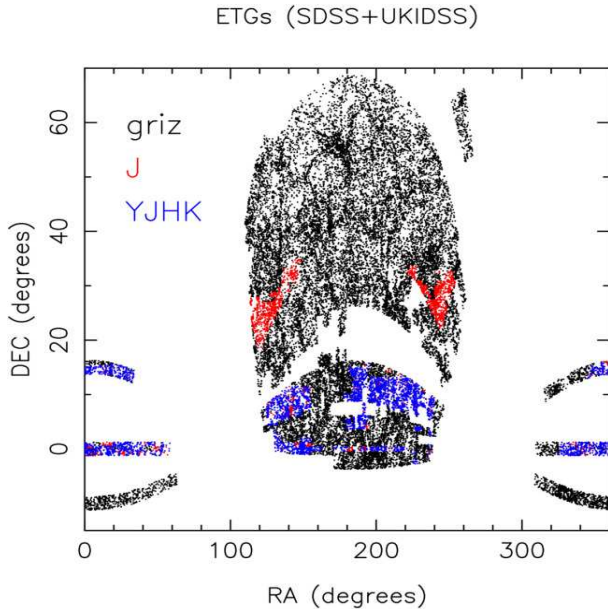
Figure 1. Distribution in RA and DEC of the SPIDER sample. Black points mark the optical $griz$ data, while red and blue symbols denote the J and $YJHK$ data, respectively. .

carried out with a resolution of $0.4\,''/pixel$, and then interleaved to a subpixel grid. This procedure results into stacked frames with a better resolution of $0.2\,''/pixel$. The $YJHK$ stacked images (multiframes) have average depths [2] of 20.2, 19.6, 18.8, and 18.2 mags, respectively. The matching of SDSS to UKIDSS data was done with the *CrossID* interface of the WFCAM Science Archive website [3]. For each ETG in the SDSS sample, we searched for the nearest UKIDSS detection within a radius of 1", by considering only UKIDSS frames with better quality flag ($ppErrBits < 16$). The matching result was very insensitive to the value of the searching radius. In fact, changing it to 0.5" leads to decrease the sample with galaxies having $YJHK$ data available by only five objects. The number of matched sources is maximum in J band, with $7,604$ matches, while amounts to $5,698$, $6,773$, and $6,886$ galaxies in Y, H, and K bands, respectively. Considering ETGs simultaneously matched with two UKIDSS bands, $H + K$ provides the maximum number of objects ($6,575$). For any possible set of three bands, the number of matches varies between $5,228$ ($Y + J + K$) to $5,323$ ($J + H + K$), which is not significantly larger than the number of $5,080$ ETGs having photometry available in all the $YJHK$ bands. For this reason, we have retrieved NIR data for only those galaxies with available photometry in either J ($7,604$), or $H + K$ ($6,575$), or $YJHK$ wavebands ($5,080$). The completeness in magnitude of each sample is characterized in Sec. 8.

In summary, the SPIDER sample includes 39,993 galaxies with available photometry and spectroscopy from SDSS-DR6. Out of them, 5,080 galaxies have NIR photometry in DR4 of UKIDSS-LAS. The distribution of galaxies with optical and NIR data on the sky is illustrated in Fig. 1.

2.2 Contamination by Faint Spiral Structures

Specification of a given family of systems means setting a property (or properties) that isolates systems that presumably went through similar evolutionary processes. However, when we select as ETGs systems with SDSS parameters $eClass < 0$ and $fracDev_r > 0.8$ we expect a certain amount of contamination by galaxies exhibiting faint structures resembling spiral arms or other non-systemic morphologies. Although several morphological indicators have been proposed from the parameters of the SDSS pipeline (e.g. Strateva et al. 2001), the eyeball classification is still considered one of the most reliable indicator despite its evident subjectivity (Weinmann et al. 2009). We have visually inspected a subsample of 4,000 randomly chosen galaxies from our sample, classifying them into three groups: *ETGs* (featureless spheroids); *face-on* LTGs - late type galaxies (a bulge surrounded by an obvious disk); and *edge-on* LTGs (a bulge with a prominent disk). This classification is then used to evaluate the ability of the different morphological indicators to distinguish edge-on and face-on galaxies from the bonafide ETGs.
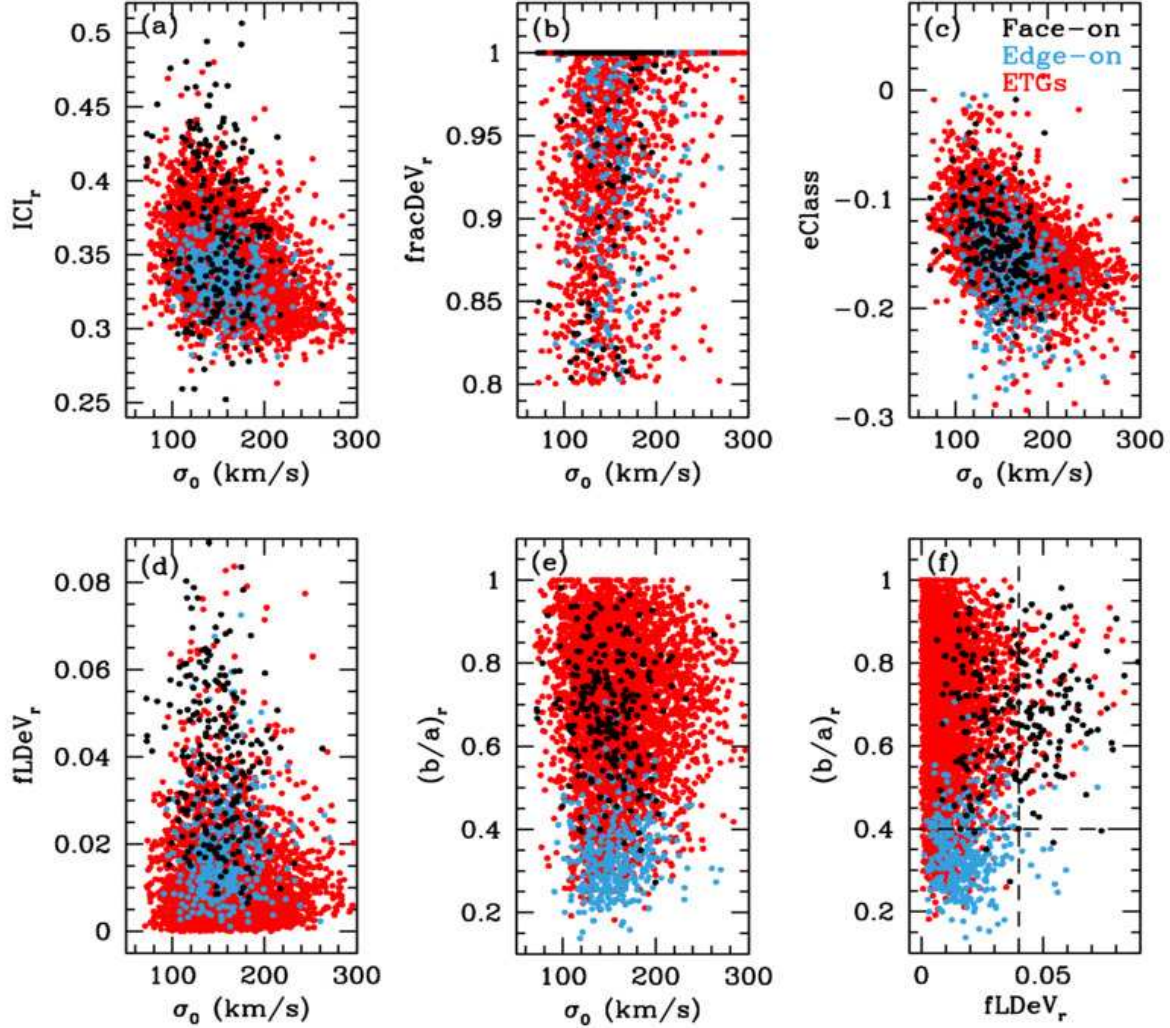
Five SDSS morphological indicators are considered as shown in Figs. 2(a-e): (i) The r-band Inverse Concentration Index (ICI_r), defined by the ratio of the 50% to the 90%-light Petrosian radii (see Shimasaku et al. 2001); (ii) The parameter $fracDeV_r$, corresponding to the fraction of the total fitted model accounted for the de Vaucouleurs component. Notice that the total fit is not a bulge+disk decomposition but a re-scaled sum of the best-fitting de Vaucouleurs and exponential components (Bernardi et al. 2006); (iii) The $eClass$ indicator (see Sec. 2.1); (iv) The fractional likelihood of a de Vaucouleurs model fit (fLDeV$_r$), defined as:

$$fLDeV_r = \frac{lnLDeV_r}{(lnLDeV_r + lnLexp_r + lnLstar)} \quad (1)$$

where $LDeV$, $Lexp$ and $Lstar$ are the probabilities of achieving the measured chi-squared for the de Vaucouleurs, exponential and PSF fits, respectively; and (v) The projected axis ratio $(b/a)_r$ of a deVaucouleurs fit (deVAB$_r$ - an SDSS attribute). From Fig. 2 fLDeV$_r$ and $(b/a)_r$ are the two better performance indicators discriminating ETGs from face-on LTGs (see Maller et al. 2009). Based on the visual inspection, we define two cutoff values (see panel f in the Figure), one for each morphology indicator, defining a region where the contamination rate is ∼5%. We notice that this contamination rate is ∼2.5 times smaller than that for the sample of 4,000. The selected values for the cutoffs are 0.04 and 0.4 for fLDeV$_r$ and $(b/a)_r$, respectively. The same constraints imposed to the entire ETG sample, define a sub-sample of 32,650 bonafide ETGs. We flag 7,343 objects as lying in the non-bonafide ETGs region defined by $(b/a)_r < 0.4$ or fLDeV$_r > 0.04$, so that we can study the impact of contaminants on the global properties of bonafide ellipticals.

3 PHOTOMETRY

For each ETG, we retrieved the corresponding best-calibrated frames from the SDSS archive and the multiframes from the WFCAM Science Archive. In the case of SDSS, only the griz images were analyzed, since the signal-to-noise of the u-band data is too low to measure reliable structural parameters. The resulting photometric system, consisting of the $grizYJHK$ wavebands, is shown in Fig. 3, where we plot, for each band, the corresponding overall transmission curve. Regarding photometric calibration, the zero–point of each image was retrieved from the corresponding SDSS or

---

[2] defined by the detection of a point source at 5σ within a $2''$ aperture.
[3] See http://surveys.roe.ac.uk/wsa/index.html for details.

Figure 2. Different morphological indicators are plotted as a function of the central velocity dispersion of the galaxy for a subsample of 4,000 ETGs (panels a-e). Panel (f) plots the two optimal indicators and the dashed lines indicate the region where the contamination is ∼6% (($b/a)_r > 0.4$ and fLDeV$_r < 0.04$. Face-on LTGs are indicated in black, edge-on LTGs in blue and bonafide ETGs in red, as shown in the upper-right corner of panel (d).

UKIDSS archives. As a result of the different conventions adopted in the two surveys, the SDSS photometry is in the AB photometric system [4], while UKIDSS data are calibrated into the Vega system (Lawrence et al. 2007).

3.1 Integrated properties

We have measured both aperture and total galaxy magnitudes with different methods, homogeneously for both the optical and NIR data. Aperture magnitudes are estimated with S-Extractor (Bertin & Arnout 1996). For each galaxy, several apertures are measured, spanning the 2 to 250 pixels diameter range. A set of adaptive aperture magnitudes is also measured. The adaptive apertures have di-

ameters of $d_k = k \cdot r_{Kr,i}$, where $k = 3, 4, 5, 6$ is a multiplicative factor, and $r_{Kr,i}$ is the Kron radius (Kron 1998) in the i-band, as estimated with S-Extractor. The $r_{Kr,i}$ is measured in i-band since this is approximately in the middle of the SPIDER photometric system (Fig. 3). For $k = 3$, the median value of d_k is ∼ $5.8''$, which is more than five times larger than the typical FWHM in all wavebands (see Sec. 3.2). More than 95% of all the ETGs have a value of d_3 larger than ∼ $4.8''$, and a ratio of d_3 to the seeing FWHM value larger than 3. This makes the adaptive aperture magnitudes essentially independent of the seeing variation from g through K (see Sec. 3.2). Different types of total magnitudes are adopted. For the optical wavebands, we retrieve both petrosian and model magnitudes, m_p and m_{dev}, from the SDSS archive (see Stoughton et al. 2002). For each waveband, the Kron magnitude, m_{Kr}, is also measured independently for all galaxies, within an aperture of three times the Kron radius in that band. The Kron magnitudes are obtained from MAG_AUTO parameter as estimated in S-Extractor.

---

[4] We actually apply small offsets to the $griz$ zero-points in order to produce a better match between the SDSS and AB systems (see www.sdss.org/dr6/algorithms/fluxcal.html#sdss2ab).
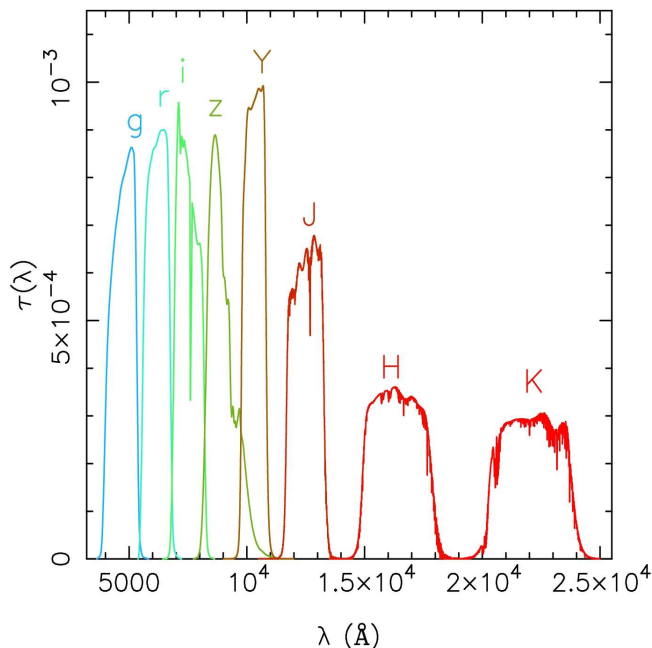
Figure 3. Transmission curves, $\tau(\lambda)$, for the $grizYJHK$ filters. Each curve has been normalized to an area of one.

Finally, each galaxy has the estimate of total magnitude, m_T, from the corresponding two-dimensional fitting model (see Sec. 3.2).

To obtain homogeneous measurements from g through K, magnitudes are k-corrected and dereddened for galactic extinction by re-computing both corrections with the same procedure in all wavebands, rather than retrieving them, when available, from the SDSS and UKIDSS archives. For each galaxy, the amount of extinction is estimated from the reddening maps of Schlegel, Finkbeiner, and Davis (1998), applying the correction of Bonifacio, Monai & Beers (2000) that reduces the color excess value, $E(B - V)$, in regions of high extinction ($E(B - V) > 0.1$). This correction is not included in the SDSS database, and only a very small fraction of ETGs ($< 1\%$) is found in the high extinction regions. We computed k-corrections using the software $kcorrect$ (BL03), through restframe filters obtained by blue-shifting the throughput curves in Fig. 3 by a factor $(1 + z_0)$. For $z_0 = 0$, one recovers the usual k-correction. For galaxies at redshift $z = z_0$, the k-correction is equal to $-2.5 \log(1 + z_0)$, independent of the filter and the galaxy spectral type. We have adopted $z_0 = 0.0725$ which is the median redshift of the ETG sample. According to BL03, this choice allows uncertainties on the k-corrections to be minimized [5]. We have tested how the waveband coverage can affect the k-corrections. For the sample of $5,080$ galaxies with available data in all $grizYJHK$ bands, we have estimated the k-corrections in $griz$ for two cases, where we used (i) all the eight wavebands and (ii) only the SDSS bands. k-corrections turned out to be very stable with respect to the adopted waveband's set, with the standard deviation of k-correction differences being smaller than $0.01mag$ for all the $griz$ wavebands.

[5] The value of $z_0 = 0.0725$ is smaller than that of $z_0 = 0.1$ adopted for sample selection (Sec. 2). The value of $z_0 = 0.1$ makes the selection more similar to that performed from previous SDSS studies, while the choice of $z_0 = 0.0725$ minimizes the errors in k-corrections.

3.2   Structural parameters

The $grizYJHK$ images were processed with 2DPHOT (La Barbera et al. 2008a) (hereafter LdC08), an automated software environment that allows several tasks, such as catalog extraction (using S-Extractor), star/galaxy separation, and surface photometry to be performed. The images were processed using two Beowulf systems. The optical images were processed at the INPE-LAC cluster facility, running 2DPHOT simultaneously on 40 CPUs. A number of $31,112$ best-calibrated frames were processed in each of the $griz$ wavebands, requiring ~ 2 days per band. The UKIDSS frames were processed at the Beowulf system available at INAF-OAC. A total of $12,963$ multiframes were processed by running 2DPHOT on 32 CPUs, simultaneously. The processing took half a day for each band.

A complete description of the 2DPHOT package can be found in LdC08; here we only outline the basic procedure followed to measure the relevant galaxy parameters. Both the optical and NIR images were processed with the same 2DPHOT setup to guarantee a homogeneous derivation of structural parameters from g through K. For each frame, the so-called *sure stars* are identified from the distribution of all the detected sources in the FWHM vs. signal-to-noise, S/N, diagram. This procedure allows an estimate of the average seeing FWHM of the image to be obtained (see sec. 3 of LdC08). For each ETG, a local PSF model is constructed by fitting the four closest stars to that galaxy with a sum of three two-dimensional Moffat functions. Deviations of the PSF from the circular shape are modeled by describing the isophotes of each Moffat function with Fourier-expanded ellipses. Galaxy images were fitted with PSF-convolved Sersic models having elliptical isophotes plus a local background value. For each galaxy, the fit provides the following relevant parameters: the effective (half-light) radius, r_e, the mean surface brightness within that radius, $<\mu>_e$, the Sersic index (shape parameter) n, the axis ratio b/a, and the position angle of the major axis, PA. The total (apparent) magnitude, m_T, of the model is given by the definition $m_T = -2.5 \log(2\pi) - 5 \log(r_e) + <\mu>_e$. Mean surface brightness values are k-corrected and corrected for galactic extinction as described in Sec. 3.1. Moreover, cosmological dimming is removed by subtracting the term $10 \log(1 + z)$, where z is the SDSS spectroscopic redshift.

The characterization of the galaxy isophotal shape is done through the two-dimensional fitting of each ETG in the gri wavebands, where Sersic models having isophotes described by Fourier-expanded ellipses are adopted. Only the fourth order *cos* term of the expansion, a_4, is considered (boxiness - $a_4 < 0$ and diskyness - $a_4 > 0$, see e.g. Bender & Möllenhoff 1987, hereafter BM87). Only the gri band images are analyzed, since a_4 is usually measured in the optical wavebands. Since the models are PSF-convolved, the method above provides a global deconvolved estimate of a_4. This estimate is somewhat different from the definition of BM87, where the peak value of a_4 is derived in a given radial range, with the minimum radius being set to four times the seeing FWHM and the maximum radius to twice the effective radius. Since many galaxies in the SPIDER sample have effective radii comparable to a few times the seeing FWHM value (see below), the BM87 procedure is not applicable.

Fig. 4 shows the distribution of the average seeing FWHM value for all the retrieved images from g through K. The seeing FWHM was estimated from the *sure star* locus (see above). For each band, we estimate the median of the distribution of FWHM values, and the corresponding width values, using the bi-weight
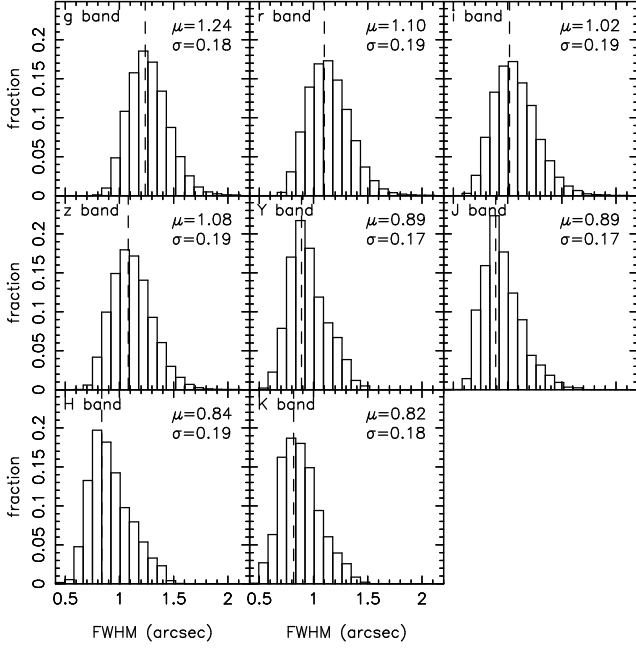
Figure 4. Distribution of seeing FWHM values for all the $grizYJHK$ frames (from left to right and top to bottom). The median value, μ, of each distribution is marked by the dashed line in each panel. Both the value of μ and the width, σ, of the distributions are reported in the top-right corner of each plot.

statistics (Beers, Flynn, & Gebhardt 1990). The median and width values are reported in Fig. 4 for each band. As expected, the median FWHM value tends to smoothly decrease from the blue to NIR wavebands, varying from $1.24''$ in g-band to $0.82''$ in K-band. This variation corresponds to a relative change of $\sim 34\%$ (with respect to g band). Notice also that in $YJHK$ ($griz$) bands almost all frames have seeing FWHM values better than $1.5''$ ($1.8''$), with 90% of the values being smaller than $1.2''$ ($1.5''$). This decreasing of the seeing FWHM from g through K matches almost exactly the relative change of effective radii from optical to NIR wavebands (see below), making the ratio of FWHM to r_e almost constant from g to K.

Fig. 5 compares the distribution of χ^2 values obtained from the two-dimensional fitting of galaxies in each band. The peak and width values of the distributions are computed by the bi-weight statistics and reported in the figure. The χ^2 is computed as follows. For each galaxy, we select only pixels 1σ above the local sky background value. The intensity value of each pixel is computed from the two-dimensional seeing-convolved Sersic model. For the selected pixels, we compute the χ^2 as the rms of residuals between the galaxy image and the model. Residuals are normalized to the expected noise in each pixel, accounting for both background and photon noise. Notice that this χ^2 computation is somewhat different from that of the two-dimensional fitting procedure, where the sum of square residuals over all the galaxy stamp image is minimized (see LdC08). This explains the fact that all the peak values in Fig. 5 are slightly larger than one. An eye inspection of the residual maps, obtained by subtracting the models to the galaxy images, shows that the above χ^2 estimate is better correlated to the presence of faint morphological features (e.g. spiral arms, disk, etc...), that are not accounted for by the two-dimensional model. This is shown in Figs. 6 and 7. Both figures show residual maps in the r-band. Fig. 6 displays cases where the χ^2 is close to the peak
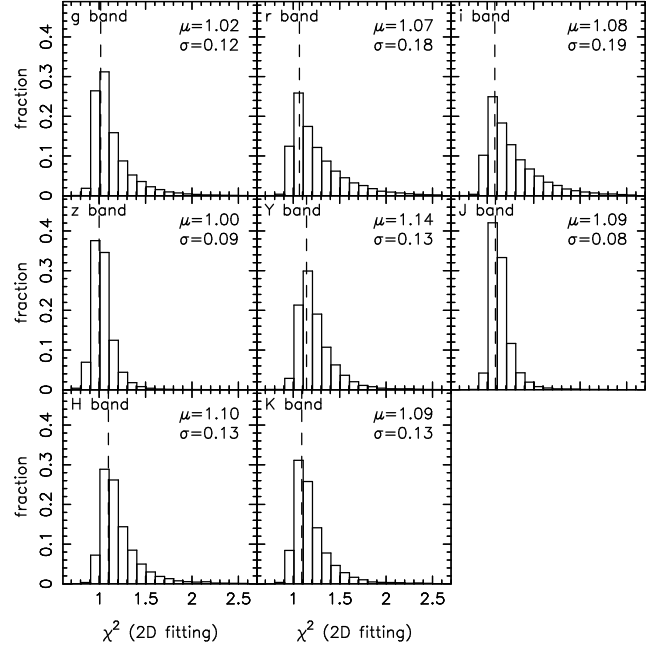

**Figure 5.** Same as Fig. 4 for the χ^2 distributions.

value ($\chi^2 < 1.5$), while Fig. 7 exhibits cases with higher χ^2 value ($1.5 < \chi^2 < 2.0$). In most cases, as the χ^2 value increases, we can see some faint features to appear in the residual maps. We found that the percentage of galaxies with $\chi^2 > 1.5$ is not negligible, amounting to $\sim 17\%$ in r-band. Most of the morphological features are expected to be caused by young stellar populations, hence disappearing when moving to NIR bands, where the galaxy light is dominated by the old, quiescent stars. From Fig. 5, one can actually see that NIR bands exhibit a less pronounced tail of positive χ^2 values with respect to the optical. This is also confirmed by a Kolmogorov-Smirnov (KS) test. For instance, in the case of r and K bands, the KS test gives a probability smaller than 1% for the corresponding χ^2 distributions to be drawn from the same parent distribution.

3.3 Uncertainty on structural parameters

We estimate the uncertainties on structural parameters by comparing the differences in $\log r_e$, $<\mu>_e$, and $\log n$ between contiguous wavebands. To obtain independent estimates of the uncertainties on SDSS and UKIDSS parameters, the comparison is performed for the r and i bands, and the J and H bands, respectively. The variation of $\log r_e$, $<\mu>_e$, and $\log n$ with waveband depends on the measurement errors on structural parameters as well as on the intrinsic variation of stellar population properties (e.g. age and metallicity) across the galaxy, which implies a change of the light profile with waveband. As it is well known, this change is responsible for the existence of radial color gradients inside ETGs (Peletier et al. 1990). The basic assumption here is that the r and i (J and H) bands are close enough that the variation of galaxy properties from one band to the other is dominated by the measurement errors. Tab. 1 shows that this is the case. In this table we report the sensitivity of color indices with respect to age and metallicity between contiguous wavebands for a Simple Stellar Population (SSP) model. The sensitivities to age and metallicities, indicated as Δ_t and Δ_Z, are defined as the derivatives of the color indices with
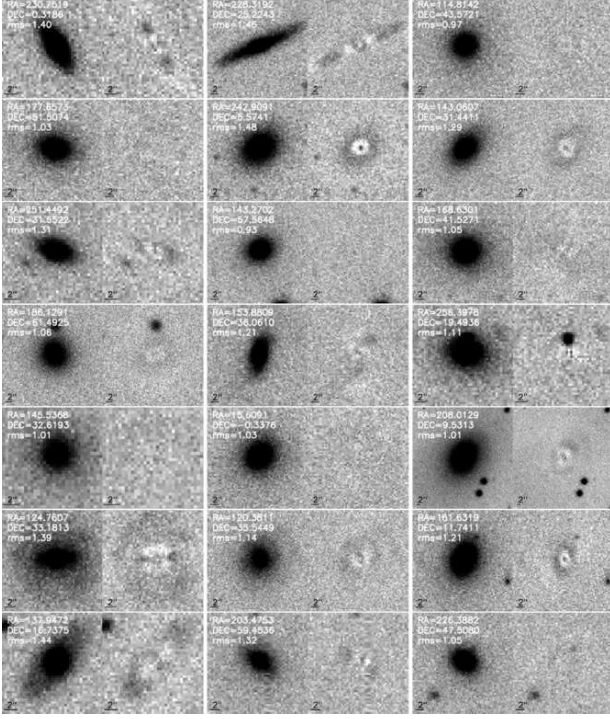
Figure 6. Two-dimensional fit results for galaxies in r-band with typical χ^2 value ($\chi^2 < 1.5$). Each plot shows the galaxy stamp (left) and the residual map (right) after model subtraction, using the same gray scale of intensity levels. The spatial scale is shown in the bottom-left corner of the left plots. For each galaxy image, the corresponding celestial coordinates (right ascension, RA, and declination, DEC, in degrees) and χ^2 value are reported in the upper-left corner.
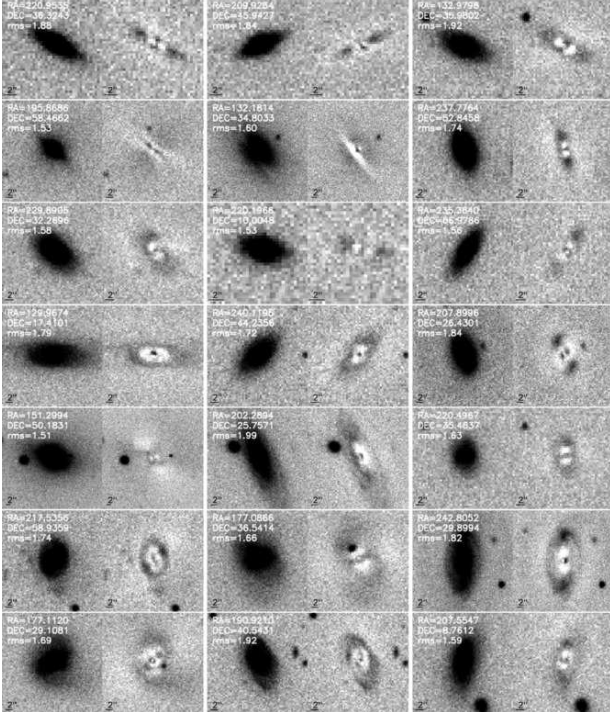
Figure 7. Same as Fig. 6 but for galaxies with high χ^2 value ($1.5 < \chi^2 < 2.0$ in r-band).

Table 1. Sensitivity of color indices of an SSP model to age and metallicity.

color index	Δ_Z	Δ_t
g-r	0.313	0.268
r-i	0.079	0.108
i-z	0.107	0.131
z-Y	0.238	0.116
Y-J	0.239	0.076
J-H	0.017	0.030
H-K	0.134	0.049

respect to $\log t$ and $\log Z$, where t and Z are the age and metallicity, respectively. The derivatives are estimated as in La Barbera & de Carvalho (2009). We use an SSP from the Bruzual & Charlot (2003) synthesis code, with solar metallicity, Scalo IMF, and an age of $t = 10.6$ Gyr, corresponding to a formation redshift of $z_f = 3$ in the adopted cosmology. For the SDSS wavebands, the sensitivities reach a minimum in $r-i$, while they have a maximum in $g-r$, as expected by the fact that this color encompasses the 4000Å break in the spectrum of ETGs at the median redshift of the SPIDER sample ($z = 0.0725$). The values of Δ_t and Δ_Z can be used to estimate the expected intrinsic waveband variation of structural parameters. As shown by Spolaor et al. (2009), bright ETGs have a large dispersion in their radial metallicity gradients, ∇_Z, with ∇_Z varying in the range of about 0 to -0.6 dex. On the contrary, age gradients play a minor role (La Barbera & de Carvalho 2009). Even considering a dispersion of 0.3 dex in the metallicity gradients of ETGs, from Tab. 1, one can see that the corresponding scatter in the $r-i$ internal color gradients would be only $0.079 \cdot 0.3 \sim 0.024$mag. Following Sparks & Jörgensen (1993), for a de Vaucouleurs profile, this implies an intrinsic scatter in the difference of r- and i-band effective radii of only $\sim 2.4\%$, hence much smaller than the typical measurement error on r_e (see below). For the UKIDSS wavebands, the lowest sensitivities to age and metallicity are obtained in $J-H$, being even smaller than those of the optical colors.

The errors on structural parameters are expected to be mainly driven by two parameters, the FWHM + pixel scale of the image (with respect to the galaxy size) and the signal-to-noise ratio, SN. Consequently, we bin the differences in $\log r_e$, $<\mu>_e$, and $\log n$ between r and i (J and H) bands with respect to the logarithm of the mean effective radius, $\log r_e$, and the SN per unit area of the galaxy image, SN/r_e^2. The SN is defined as the mean value, between the two bands, of the inverse of the uncertainties on Kron magnitudes. Each bin is chosen to have the same number of galaxies. In a given bin, we estimate the measurement errors on $\log r_e$, $<\mu>_e$, and $\log n$ from the mean absolute deviation of the corresponding differences in that bin. We refer to the measurement uncertainties as $\sigma_{\log r_e}$, $\sigma_{<\mu>_e}$, and $\sigma_{\log n}$, respectively. Since the errors on effective parameters are strongly correlated, we also derive the corresponding covariance terms, $COV_{Y,X}$, in each bin, where X and Y are two of the three quantities $\log r_e$, $<\mu>_e$, and $\log n$. For each pair of X and Y, we perform a robust linear fit [6] of the differences in Y as a function of the corresponding differences in X. The quantity $COV_{Y,X}$ is obtained from the slope, s, of the fitted relation as $COV_{Y,X} = s \times \sigma_X^2$, with the constraints $|COV_{Y,X}| \leqslant \sigma_Y \times \sigma_X$, and $COV_{Y,X} = COV_{X,Y}$. Fig. 8 plots the

---

[6] The robust regression is performed by minimizing the sum of absolute residuals of the Y vs. the X differences.
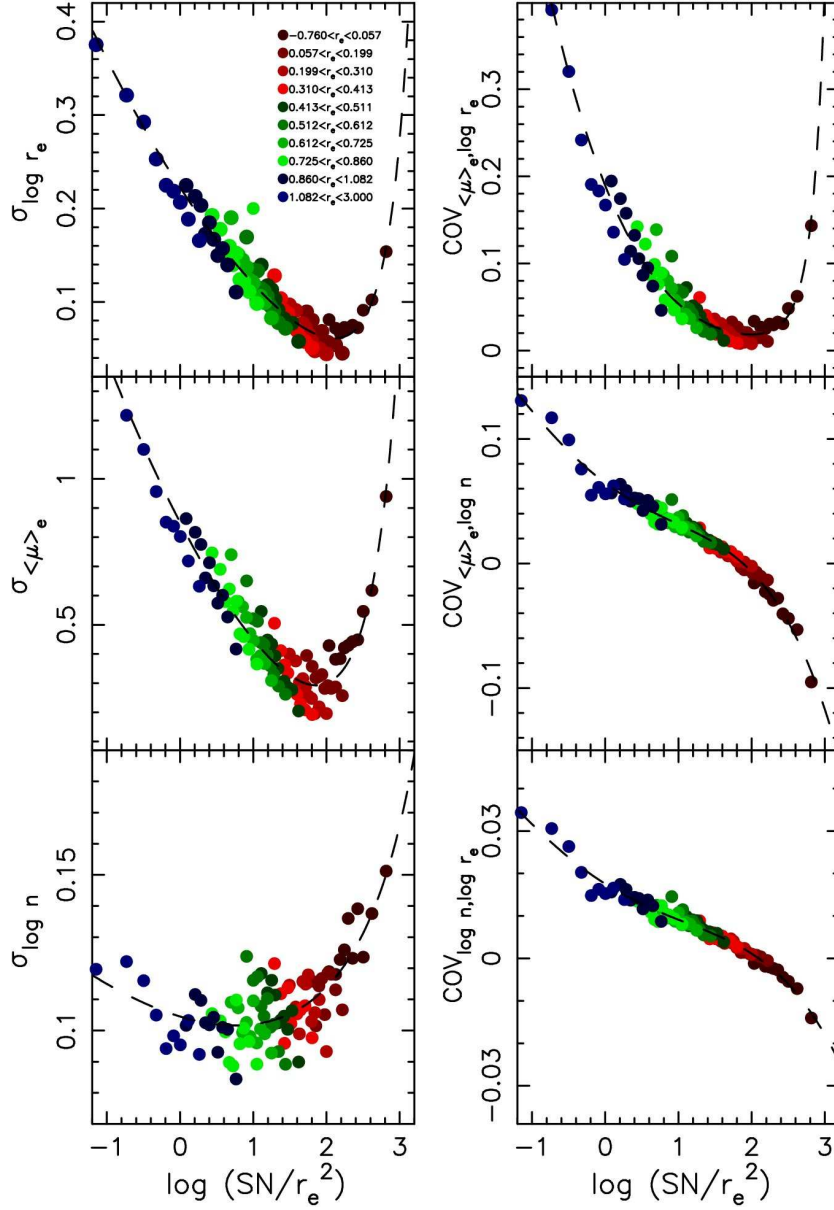
Figure 8. Errors on optical effective parameters as a function of the logarithm of the signal-to-noise (SN) per pixel. In the left panels, from top to bottom, we plot the uncertainty on the effective radius, the effective mean surface brightness, and the Sersic index. The left panels, from top to bottom, plot the covariance terms of the uncertainties on $\log r_e$, $<\mu>_e$, and $\log n$. Different colors show different bins of the effective radius as shown in upper-right of the top-left panel. For a given color, the points shows the values of the uncertainties and the covariance terms obtained in different bins of the logarithm of the SN per pixel. The dashed curves are the best-fit functional forms used to model the dependence of the uncertainties on SN (see the text).

quantities $\sigma_{\log r_e}$, $\sigma_{<\mu>_e}$, and $\sigma_{\log n}$ as well as the relevant covariance terms as a function of $\log(SN/r_e^2)$, for the r and i bands. The errors on effective parameters are strongly correlated to the SN per unit area. For $\log(SN/r_e^2)\widetilde{<}2$, as the signal-to-noise per unit area decreases, the errors tend to become larger. For $\log(SN/r_e^2)\widetilde{>}2$, all galaxies have effective radii comparable or even smaller than the pixel scale, with large values of $\log(SN/r_e^2)$ corresponding to smaller effective radii. As a result, the error on the effective parameters tends to increase as well. The $\sigma_{\log n}$ exhibits a similar behavior to that of $\sigma_{\log r_e}$ and $\sigma_{<\mu>_e}$, though with a larger dispersion at given $\log(SN/r_e^2)$. For the errors on effective parameters ($\sigma_{\log r_e}$, $\sigma_{<\mu>_e}$, and $COV_{\log r_e, <\mu>_e}$) and Sersic index ($\sigma_{\log n}$), the trends

exhibited in Fig. 8 are well described by the following, empirical functional form:

$$y = P_2(x) + \frac{|c_1|}{(x-5)^{c_2}}, \qquad (2)$$

where y is one of the quantities $\sigma_{\log r_e}$, $\sigma_{<\mu>_e}$, and $COV_{\log r_e, <\mu>_e}$, $x = \log(SN/r_e^2)$, P_2 is a second order polynomial function, while c_1 and c_2 are two parameters describing the increase of the error values at high SN per unit area. For the quantities $COV_{<\mu>_e, \log n}$ and $COV_{\log n, \log r_e}$, the trends in Fig. 8 can be modeled by a fourth order polynomial function. We have fitted the corresponding functional forms by minimizing the sum of absolute residuals in y. The best-fit curves are exhibited in Fig. 8.

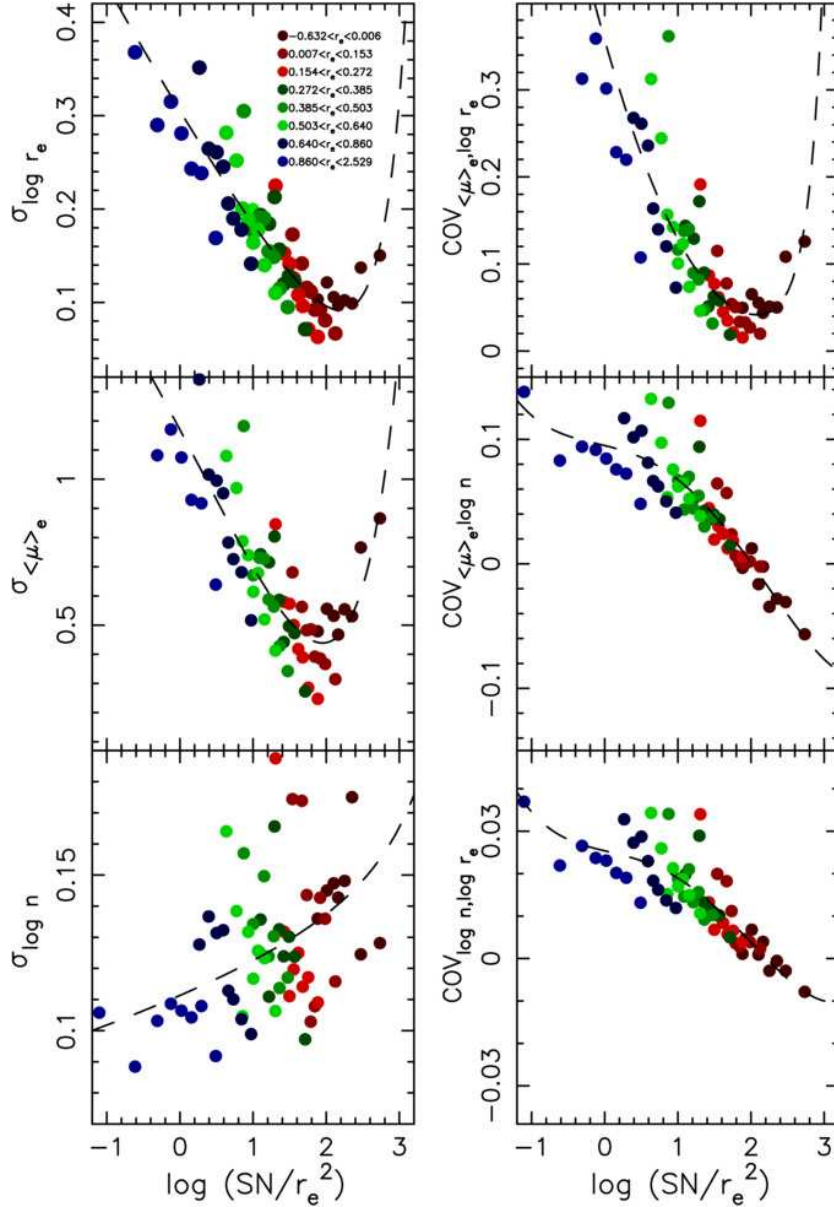Fig. 9 plots the errors on structural parameters as derived with

Figure 9. Same as Fig. 8 but comparing J and H band structural parameters.

the above procedure for the J and H bands. The trends are similar to those obtained for the optical parameters, but with a larger dispersion, at given SN per unit area, which is likely explained by the fact that the number of galaxies in each bin with available photometry in J and H is smaller (by a factor of ~ 8) than that in r and i. The uncertainties on the NIR parameters are on average larger than those in the optical. For instance, at $\log(SN/r_e^2) = 2$, the uncertainty on $\log r_e$ is ~ 0.06 dex in the optical, increasing to ~ 0.1 dex in the NIR. The median errors on $\log r_e$, $< \mu >_e$, and $\log n$, amount to ~ 0.1, ~ 0.5 $mag/arcsec^2$, and ~ 0.1, respectively, in the optical, and to ~ 0.15, ~ 0.6 $mag/arcsec^2$, and ~ 0.12 in the NIR. This difference can be qualitatively explained by the fact that (i) the stars used for the PSF modeling have, on average, a lower signal-to-noise ratio in the NIR than in the optical, and (ii) that the ratio of galaxy effective radii to the pixel scale of the images is smaller in the NIR than in the optical. The trends in

Fig. 9 are modeled with the same functional forms as for the optical data.

We use the above analysis to assign errors to the structural parameters to each galaxy in the SPIDER sample, for each waveband. For a given galaxy, we first calculate its SN per unit area and then use the best-fitting functional forms to assign $\sigma_{\log r_e}$, $\sigma_{<\mu>_e}$, $\sigma_{\log n}$, and the corresponding covariance terms. For the gri bands, we adopt the functional forms obtained from the $r - i$ comparison, while for the JHK bands we adopt the values obtained from the comparison of J- and H-band parameters. In the z and Y bands, we apply both the optical and NIR functional forms, and then derive the errors by interpolating the two error estimates with respect to the effective wavelength of the passbands.

4   COLOR-MAGNITUDE RELATIONS

As a first step in the comparison of optical to NIR properties of ETGs, we start to analyze the differences in their integrated properties, i.e. the color indices. The goal is comparing total Sersic magnitudes in the different wavebands, in order to (i) characterize the completeness of the SPIDER sample in the space of the (Sersic) effective parameters (Sec. 8), and (ii) select suitable samples of ETGs for the analysis of the FP (see papers II and III). Thus, we estimate the color indices using the Sersic total magnitudes, rather than aperture magnitudes as in most of previous studies, and refer to them also as the *total* galaxy colors. This is by itself an important issue that will be addressed in a future contribution dealing with the different ways of measuring colors (de Carvalho et al. 2010, in preparation) which certainly goes beyond the scope of this paper.

The comparison of color indices is performed by constructing the color–magnitude diagrams for different pairs of wavebands. Since the ETG sample has photometry available in eight wavebands, we can derive seven different color–magnitude relations. We consider galaxy colors in the form of $g - X$ with $X = rizYJHK$, and we write the color magnitude relations as:

$$g - X = a_{gX} + b_{gX}X, \qquad (3)$$

where a_{gX} and b_{gX} are the offsets and slopes of the relations. To simplify the notations, we also set $a_{gg} = 0$ and $b_{gg} = 0$. Fig. 10 plots the CM diagrams for all the $5,080$ ETGs with available data in all wavebands. In order to derive a_{gX} and b_{gX}, we first bin each $g - X$ vs. X diagram with respect to the magnitude X. We adopt $N = 15$ bins, with each bin including the same number of galaxies. Varying the number of bins in the range of 15 to 25 changes the slope and offset values by less than 1%. For each bin, we derive the peak of the corresponding distribution of galaxy colors by applying the bi-weight location estimator (Beers, Flynn, & Gebhardt 1990). The uncertainty of the peak value is estimated as the standard deviation of the peak values obtained in 1000 bootstrap iterations. This procedure has the advantage of being insensitive to outliers in the color distribution. The binning is performed up to a magnitude limit X, obtained by transforming the 2DPHOT r-band completeness limit of -20.55 (Sec. 8.1) through the median values of the $g - X$ total colors. The values of a_{gX} and b_{gX} are then derived by fitting the binned values of $g - X$ vs. X, with an ordinary least-squares fitting procedure with $g - X$ as dependent variable. The uncertainties on a_{gX} and b_{gX} are obtained by randomly shifting ($N = 1000$ times) the binned values of $g - X$ according to their uncertainties. The values of a_{gX} and b_{gX} are exhibited in Fig. 10. It is interesting to notice that, using total colors, the CM relations are essentially flat, with the slopes b_{gX} being mostly consistent with zero within the corresponding uncertainties. In particular, the value of b_{gX} is consistent with zero at less than 2σ in $g - r$, $g - i$, $g - J$, $g - H$, and $g - K$, while in $g - z$ and $g - Y$ the slopes differ from zero at $\sim 3\sigma$ and $\sim 5\sigma$ levels, respectively. We do not find here any systematic steepening of the CM relation when enlarging the waveband baseline from $g - r$ to $g - K$, as expected if the *total* CM relation would be purely driven by a mass–metallicity relation in ETGs. Following Scodeggio (2001), we can explain this surprising result by the fact that we use total color indices. ETGs have negative color gradients, with color indices becoming bluer from the galaxy center to its periphery. As a result, when adopting colors in a fixed aperture, one is measuring the color inside a smaller region (with respect to r_e) for the brightest (hence larger) galaxies than for faintest galaxies in the sample. This leads to a misleading steepening of the CM relation. We notice that using de Vaucouleurs model

Table 2. Median peak values, a_{g-X}, of the distributions of total colors, $g - X$ ($X = rizYJHK$). The uncertainties are 1σ standard errors on the median values.

color	peak value
$g - r$	0.852 ± 0.007
$g - i$	1.274 ± 0.004
$g - z$	1.589 ± 0.008
$g - Y$	2.282 ± 0.012
$g - J$	2.806 ± 0.012
$g - H$	3.472 ± 0.012
$g - K$	3.854 ± 0.018

magnitudes from SDSS would essentially lead to the same effect, as model magnitudes are estimated in a fixed aperture for all the SDSS wavebands (see Stoughton et al. 2002), and the SDSS effective radii tend to be more underestimated (with respect to the Sersic r_e) for brighter than for fainter galaxies (see Fig. 16 of Sec. 6). Since the values of $b_{gX} = 0$ are mostly consistent with zero and our aim here is that of relating total magnitudes among different wavebands (rather than performing a detailed study of CM relations), we have decided to set $b_{gX} = 0$, and derive a_{g-X} as the median of the $g - X$ peak values in the different magnitude bins. The values of a_{g-X}, together with the corresponding uncertainties, are listed in Tab. 2. The uncertainties are the errors on the median values. They are estimated from the width of the distribution of median values for 200 bootstrap iterations.

Fixing the limiting magnitude of the ETG's sample in a given band, W ($W = grizYJHK$), one can use the CM relations to map that limit into *equivalent* magnitude limits, X_{lim} ($X = grizYJHK$), in all wavebands. From Eq. 3, one obtains:

$$X_{lim} = \frac{a_{gW} - a_{gX}}{1 + b_{gX}} + \frac{1 + b_{gW}}{1 + b_{gX}}W_{lim}. \qquad (4)$$

In the particular case of $b_{gX} = 0$, one obtains the simplified expressions, $X_{lim} = a_{gY} - a_{gX} + Y$, which is used in paper II to analyze the FP relation for *color–selected* samples of ETGs.

5   DISTRIBUTION OF STRUCTURAL PARAMETERS FROM g THROUGH K

Figures 11 to 13 exhibit the distributions of 2DPHOT Sersic parameters from g through K. For each band, we select all the galaxies available in that band (see Sec. 2). Each distribution is characterized by its median value, μ, and the width, σ, estimated by the bi-weight statistics (Beers, Flynn, & Gebhardt 1990). Both values, μ and σ, are reported in the plots.

Fig. 11 compares the distributions of effective radii. The most noticeable feature is that the median value of $\log r_e$ decreases smoothly from the optical to the NIR, varying from ~ 0.53 dex ($r_e \sim 3.4''$) in g to ~ 0.38 dex in K ($r_e \sim 2.4''$). This change of ~ 0.15 dex corresponds to a relative variation of $\sim 35\%$ in r_e, and is due to the fact that ETGs have negative internal color gradients, with the light profile becoming more concentrated in the center as one moves from shorter to longer wavelengths. Had we used the peak values of the distributions, estimated with the bi-weight statistics, rather than median values, the relative variation in r_e would have been $\sim 31\%$ (~ 0.13 dex) instead of $\sim 35\%$. The optical–NIR difference in $\log r_e$ is in agreement with the value of
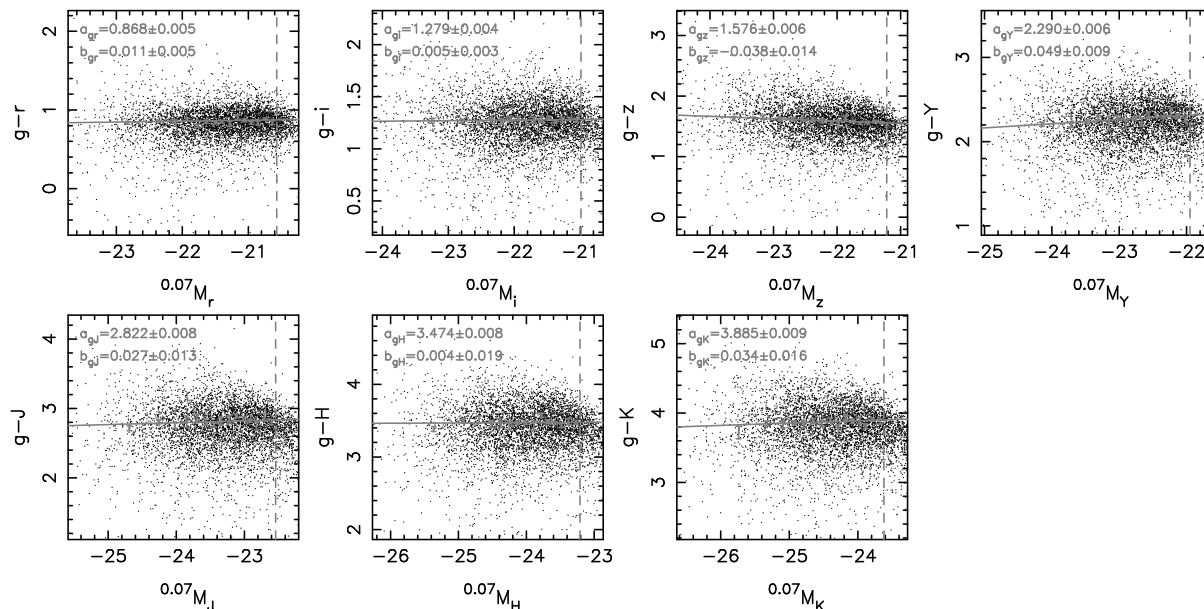
Figure 10. Color–magnitude relations for all the $5,080$ galaxies with photometry available in $grizYJHK$. From left to right and top to bottom, galaxy colors in the form of $g - X$, with $Z = rizYJHK$, are considered. For each panel: the slope and offset of the CM relation are reported in the upper-left corner, with the corresponding 1σ standard uncertainties; the colored circles mark the peak of the color distribution in magnitude bins, with the corresponding 1σ error bars; the solid line shows the best-fitting CM relation; the dashed line mark the magnitude cut ion that band that corresponds to a magnitude limit of -20.55 in the r-band (see text).

~ 0.125 dex ($\sim 29\%$) reported by Ko & Im (2005) for the sample of 273 ETGs from Pahre (1999), between the V and K bands. Notice also that the relative change in r_e fortuitously matches the improvement in average seeing FWHM between the g- and K-band images (Sec. 3.2), which makes the measurement of structural parameters across the SPIDER wavelength baseline even more homogeneous.

Fig. 12 compares the distributions of values of the axis ratio, b/a, of the best-fitting Sersic models. The median as well as the width values of b/a turn out to be essentially constant from g through K, amounting to ~ 0.7 and ~ 0.2, respectively. The consistency of the b/a distributions with wavebands is in agreement with that found by Hyde & Bernardi (2009) when comparing g- and r- bands b/a values from SDSS. As expected, the fraction of ETGs decreases dramatically at low values of b/a with only a few percent of galaxies having axis ratios as low as 0.3.

Fig. 13 compares the distributions of the Sersic index, n. Since we have selected bulge-dominated galaxies ($fracDev_r > 0.8$, see Sec. 2), all the objects exhibit a Sersic index value larger than one, i.e. no galaxy has an exponential (disk-like) light profile. In particular, the fraction of ETGs becomes significantly larger than zero above the value of $n \sim 2$, which, according to Blanton et al. (2003b), roughly corresponds to the separation limit between blue and red galaxies in the SDSS. The distributions show a large scatter, with n ranging from ~ 2 to ~ 10. The median value of n is around 6 for all wavebands, without any sharp wavelength dependence. On the other hand, we see some marginal change in the shape of the distribution with waveband. In the optical gri wavebands, a peak in the distribution is evident around $n \sim 4$. The distributions become essentially flat in the other (NIR) wavebands, with the exception of J where a peak is still present at $n \sim 4$. Some caution goes in interpreting these changes in shape. First, notice that observations and data reduction in the J-band of UKIDSS-LAS are carried out in a somewhat different manner with respect to the other wavebands
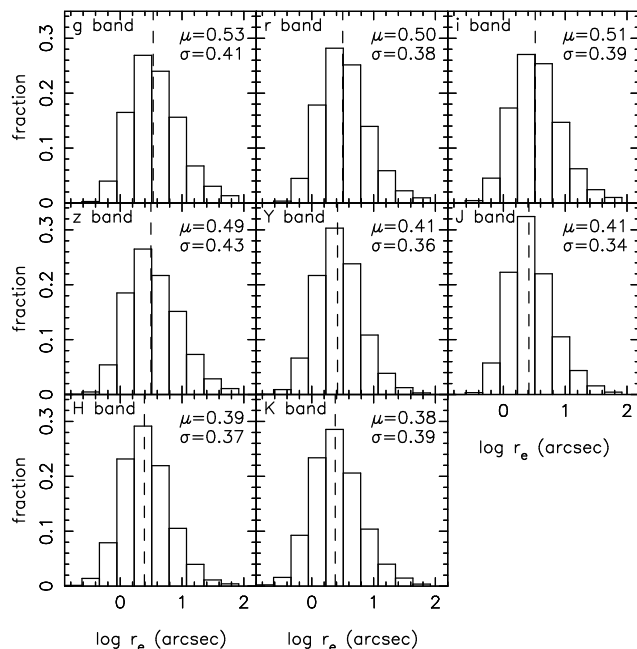

Figure 11. Distributions of $\log r_e$ for all the $grizYJHK$ wavebands (from left to right and top to bottom). The median value, μ, of each distribution is marked by the vertical dashed line. The μ and width values (see the text) are reported in the upper–right corner of each panel.

(see Warren et al.2007). A micro-stepping procedure, with integer pixel offsets between dithered exposures is performed. Images are interleaved to a subpixel grid and then stacked. This procedure results in a better image resolution of $0.2''/pixel$, with a better accuracy of the astrometric solution (useful for proper motion's measurements). We cannot exclude that this difference in data reduc-
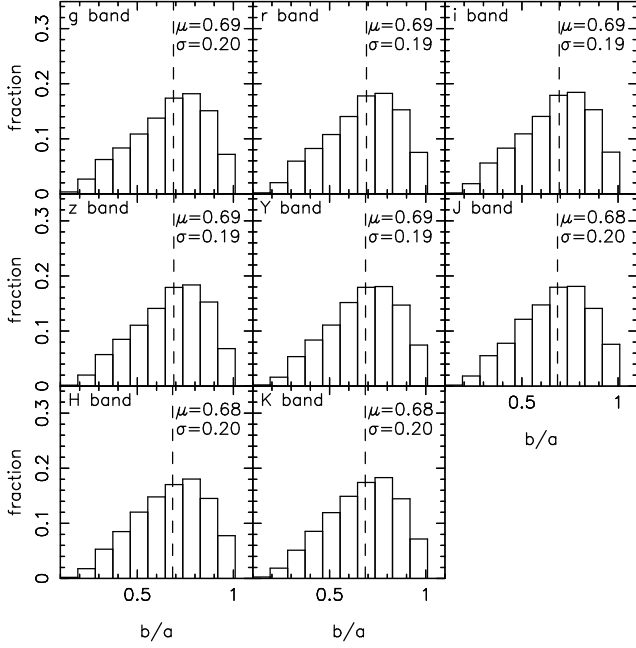
Figure 12. Same as Fig. 11 for the distribution of axis ratios.
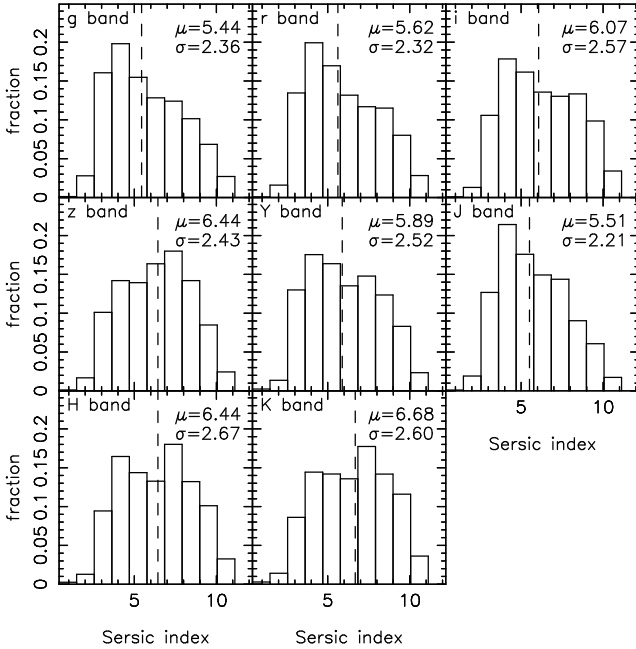
Figure 13. Same as Fig. 11 for the distribution of Sersic indices.

tion affects the J-band distribution of n values. Moreover, as seen in Sec. 3.3, uncertainties on structural parameters change from g through K, hence preventing a straightforward comparison of the shape of the distributions among different wavebands.

In order to analyze the waveband dependence of the a_4 parameter, we compare the a_4 values among contiguous wavebands for the sample of 39,993 ETGs. The comparison is performed using only the gri wavebands, where the a_4 estimates are derived (see Sec. 3.2). Fig. 14 plots the differences in a_4, δa_4, between g and r, and r and i, as a function of the median a_4 value, $< a_4 >$. The δa_4 values are binned with respect to $< a_4 >$, with each bin including
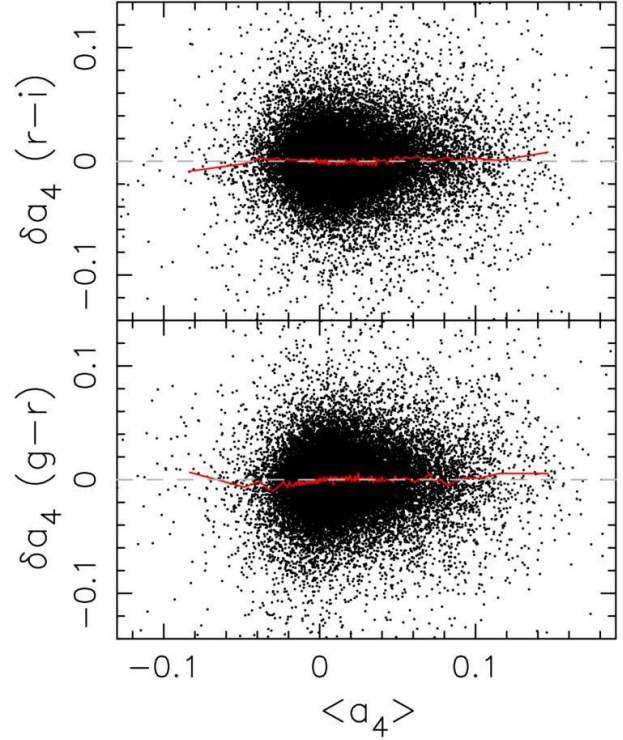
Figure 14. Differences of a_4 estimates between $r - i$ (upper panel) and $g - r$ (lower panel) as a function of the median a_4 value, $< a_4 >$, in the gri wavebands. The blue dashed line marks the value of zero. The red curves are obtained by binning the data with respect to $< a_4 >$.

the same number ($N = 200$) of galaxies. For a given bin, the median difference of δa_4 values is computed. The median values are plotted as a continuous curve in Fig. 14, showing that there is no systematic trend of a_4 from g through i.

6   COMPARISON OF SDSS AND 2DPHOT STRUCTURAL PARAMETERS

We compare the effective parameters measured with 2DPHOT with those derived from the SDSS photometric pipeline *Photo*, that fits galaxy images with two-dimensional seeing convolved de Vaucouleurs models (Stoughton et al. 2002). From now on, the differences are always in the sense of SDSS$-$2DPHOT. The comparison is done in r-band, by using the entire SPIDER sample of 39,993 ETGs (Sec. 2). Effective radii along the galaxy major axis are retrieved from the SDSS archive, and transformed to equivalent (circularized) effective radii, r_e, with the axis ratio values listed in SDSS. The effective mean surface brightness, $< \mu >_e$, is then computed from the circularized effective radii and the de Vaucouleurs model magnitude, $m_{dev,r}$, using the definition $< \mu >_e = m_{dev,r} + 5 \log(r_e) + 2.5 \log(2\pi)$. All magnitudes are dereddened for galactic extinction and k-corrected (see Sec. 3.1). For both 2DPHOT and *Photo*, we denote the effective parameters as r_e and $< \mu >_e$, saying explicitly when we refer to either one or the other source.

In order to compare the method itself to derive r_e and $< \mu >_e$ (rather than the kind of model, i.e. Sersic vs. de Vaucouleurs), we start by comparing the effective parameters of galaxies for which 2DPHOT gives a Sersic index of $n \sim 4$. To this effect, we select all the ETGs with n in the range of 3.7 to 4.3, considering only
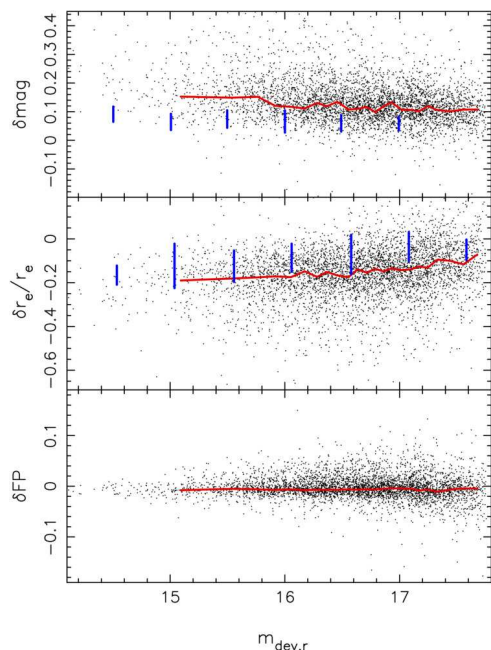
Figure 15. Differences in total magnitude, $\delta\,mag$ (upper panel), effective radius, $\delta r_e/r_e$ (middle panel), and *FP* parameter, δFP (lower panel), between SDSS and 2DPHOT, as a function of the SDSS r-band model magnitude. All values refer to the r-band. Red curves are obtained by binning the differences with respect to $m_{dev,r}$ (see the text). The blue bars mark the range of expected differences due to the sky overestimation effect present in the SDSS parameters estimation. The size of the blue bars has been estimated from fig. 6 of Abazajian et al. (2009) for δmag and fig. 3 of Adelman-McCarthy et al. (2008) for $\delta r_e/r_e$.

Figure 16. Comparison of SDSS and 2DPHOT parameters as a function of the 2DPHOT Sersic index (left panels), and the SDSS total model magnitude (right panels). From top to bottom, the same quantities as in Fig. 15 are compared. The red curves are obtained by binning the data as in Fig. 15, but with each bin including 400 galaxies.

galaxies with better quality images (seeing FWHM $< 1.5''$). This selection results into a subsample of $4,525$ ETGs. Fig. 15 plots the differences in the total magnitude, effective radius, and *FP* parameter as a function of $m_{dev,r}$, where $FP = \log r_e - 0.3 < \mu >_e$ is the combination of $\log r_e$ and $< \mu >_e$ entering the FP relation (Saglia et al. 2001). For the r_e, we normalize the differences to the *Photo* r_e values. For each quantity, the differences are binned with respect to $m_{dev,r}$, each bin including the same number ($N = 200$) of galaxies. In a given bin, the peak value of the distribution of differences (red curves in the figure) is computed by the bi-weight statistics (Beers, Flynn, & Gebhardt 1990). The SDSS total magnitudes and effective radii differ systematically from those obtained with 2DPHOT, with total magnitudes (effective radii) being fainter (smaller) with respect to those of 2DPHOT. This effect tends to disappear for faint galaxies: the absolute differences in total magnitude decrease from ~ 0.15mag ($\sim 20\%$) at $m_{dev,r} \sim 15$ to ~ 0.1mag (6%) at $m_{dev,r} \sim 17.7$. These differences are in the same sense as those reported from previous studies (e.g. Bernardi et al. 2007, Lauer et al. 2007), and can at least partly be accounted by the sky overestimation problem affecting SDSS model parameters (Adelman-McCarthy et al. 2008; Abazajian et al. 2009). *Photo* tends to overestimate the sky level near large bright galaxies, leading to underestimate both total fluxes and effective radii. The effect has been quantified from the SDSS team by adding simulated $r^{1/4}$ seeing-convolved models to SDSS images, and recovering their input parameters through *Photo*. Fig. 15 compares the range of values for differences between input and output parameters from the SDSS simulations (blue bars), with what we find here. For r_e, the average *Photo*-2DPHOT differences are only marginally consistent
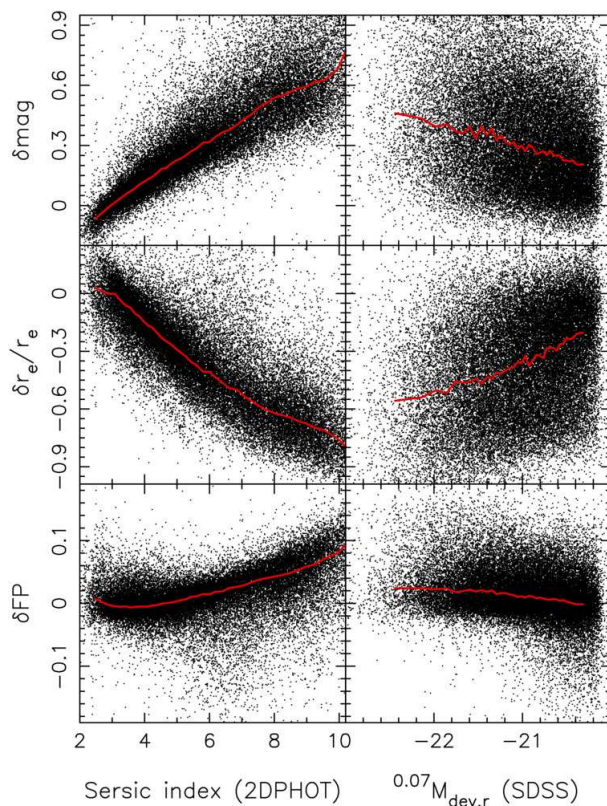
with those expected from the simulations. For the total magnitudes, we find larger systematic differences, with 2DPHOT magnitudes being brighter, by a few tenths of mag, than what expected from the simulation's results. We should notice that larger differences in magnitude (and perhaps in r_e), in the same sense as we find here, have also been reported by D'Onofrio et al. (2008) when comparing their effective parameters with those from SDSS. Moreover, the SDSS simulations have been performed by assuming a given luminosity–size relation for ETGs, which might be slightly different for ETG's samples selected according to different criteria. Since one main goal of the SPIDER project is that of analyzing the FP relation, we have to point out that, although the differences in r_e and m_T are significant, the FP quantity is in remarkable good agreement when comparing *Photo* to 2DPHOT. The average difference in the FP is less than a few percent and does not depend on the magnitude. As a consequence (see paper II), the FP coefficients change by only a few percent when using either 2DPHOT or *Photo* effective parameters.

Fig. 16 compares differences between *Photo* and 2DPHOT parameters as a function of the Sersic index, n, as well as the (SDSS) absolute model magnitude in r band, $^{0.07}M_{dev,r}$. Differences are binned as in Fig. 15, considering only the $N = 39,091$ galaxies with better image quality (see above). The comparison reveals large systematic differences, that strongly correlate with the Sersic index n. As n increases, Sersic total magnitudes become brighter – while Sersic effective radii become larger – than the SDSS values. The former trend is consistent with that reported

by Graham et al. (2005). Similar, but weaker, trends are also present as a function of the galaxy magnitude, when moving from fainter to brighter galaxies. This is somewhat expected, as ETGs exhibit a luminosity-Sersic index relation, with brighter galaxies having on average larger n (Caon, Capaccioli & D'Onofrio 1993). The trends of Fig. 16 are similar to those obtained by D'Onofrio et al. (2008) (see their fig. 1), when comparing Sersic effective parameters to the *Photo* quantities. As noticed above, the FP parameters are more stable with respect to the fitting procedure than the other quantities. In particular, the quantity FP shows only a weak dependence on galaxy magnitude (see lower-right panel of Fig. 16), with an end-to-end average variation of only 0.02 dex ($\sim 5\%$). Since the FP can be seen as a linear relation between the FP quantity and velocity dispersion (or galaxy magnitude [7], through the Faber–Jackson relation), the weak dependence of the FP quantity with magnitude implies that the coefficients of the FP are expected not to change significantly when using either 2DPHOT or SDSS parameters (see paper II).

7 SPECTROSCOPY

7.1 Velocity dispersions from SDSS and STARLIGHT

We have re-computed central velocity dispersions for all the ETGs in the SPIDER sample. Velocity dispersions are usually measured by comparing the observed galaxy spectrum with single spectral templates, which are assumed to describe the dominant stellar population of the galaxy. For ETGs, the spectra of red giant stars are usually adopted. On the other hand, ETGs frequently show mixed stellar populations, and this might significantly affect the σ_0 estimate for some fraction of the ETG's population. We derive the σ_0's with the same procedure as in the SDSS-DR6 pipeline, i.e. the direct fitting of galaxy spectra (see Adelman-McCarthy et al. 2008), but instead of using single spectral templates as in the SDSS pipeline, we construct a mixed-population spectral template for each galaxy. This is done as part of the automatic procedure described in STARLIGHT (Cid Fernandes et al. 2005) where velocity dispersion and stellar population parameters are determined simultaneously. Hence, the new velocity dispersion values should be virtually unaffected by the different kinematics of the various stellar components.

For each galaxy, we run the spectral fitting code STARLIGHT (Cid Fernandes et al. 2005) to find the combination of single stellar population (SSP) models that, normalized and broadened with a given sigma, best matches the observed spectrum (also normalized), which is first de-redshifted and corrected for extinction. We use SSP models from the MILES galaxy spectral library, with a Salpeter Initial Mass Function truncated at lower and upper cutoff mass values of 0.01 and 120 $M_\odot$, respectively (Vazdekis et al. 2010). These models are based on the MILES stellar library (Sánchez-Blázquez et al. 2006), which has an almost complete coverage of stellar atmospheric parameters at a relatively high and nearly constant spectral resolution of 2.3Å (FWHM). This resolution is better than that of SDSS spectra, allowing us to suitably degrade the spectral models to match the resolution of the observed spectra (see below).

One main issue for the estimate of velocity dispersions from
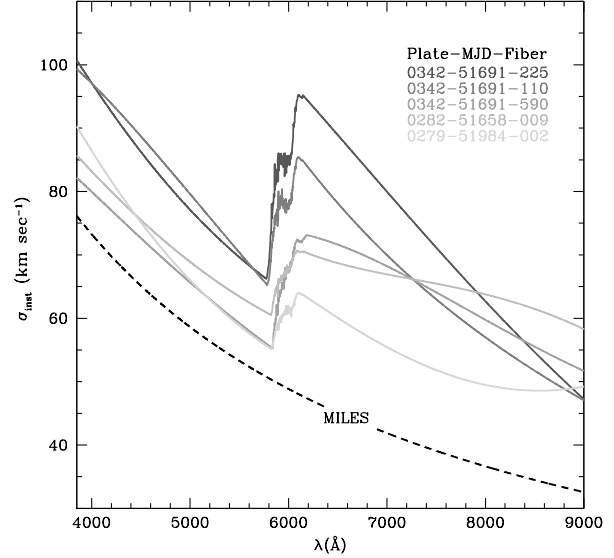
Figure 17. Wavelength dependent instrumental resolution for the SDSS spectra of five randomly selected ETGs. The resolution values are taken from the fits spectral files in the SDSS archive. The dashed line shows the resolution variation for the MILES SSP-models, which have a nearly constant value of 2.3Å (FWHM). For each galaxy, we degrade the MILES models (dashed curve) to match the corresponding wavelength dependent resolution (solid curves; see the text).

SDSS is the wavelength variation of the SDSS spectral resolution. For the ETG's spectra of the SPIDER sample, we found that the median value of the resolution varies from ~ 2.8Å (FWHM) ($\sigma_{inst} \sim 90$ km/s) in the blue (4000Å) up to ~ 3.7Å (FWHM) ($\sigma_{inst} \sim 55$ km/s) in the red (8000Å). Resolution also varies significantly among different spectra, as seen in Fig. 17, where we plot the σ_{inst} as a function of wavelength for the spectra of five randomly selected ETGs. Bernardi et al. (2003a) have accounted for the wavelength dependence of the SDSS spectral resolution by modeling it with a simple linear relation. On the contrary, in the present study, we do not perform any modeling of σ_{inst}. For each galaxy in the SPIDER sample, we degrade the SSP models to match the wavelength-dependent resolution, $\sigma_{inst}(\lambda)$, of the corresponding spectrum. The σ_{inst} is measured from the SDSS pipeline by using a set of arc lamps, and provided in one fits extension of the spectrum fits file (see Stoughton et al. 2002). The MILES models are degraded by the transformation:

$$M_s(\lambda) = \int M(x)G(x - \lambda)dx \qquad (5)$$

where $M(\lambda)$ is a given SSP model, $M_s(\lambda)$ is the smoothed model, and the function $G(\lambda)$ is a Gaussian kernel whose width is obtained by subtracting in quadrature the MILES resolution to the de-redshifted resolution $\sigma_{inst}(\lambda/(1+z))$, where z is the galaxy spectroscopic redshift. The integral is performed by discrete integration. Notice that Eq. 5 reduces to a simple convolution in the case where σ_{inst} is a constant. For each galaxy, we run STARLIGHT using the corresponding smoothed MILES models. We use a set of SSP models covering a wide range of age and metallicity values (with fixed solar [α/Fe]=0 abundance ratio). Age values range from 0.5 to ~ 18 Gyr, while metallicity values of $\log Z/Z_\odot = -1.68, -1.28, -0.68, -0.38, 0., 0.2$ are considered, resulting in a
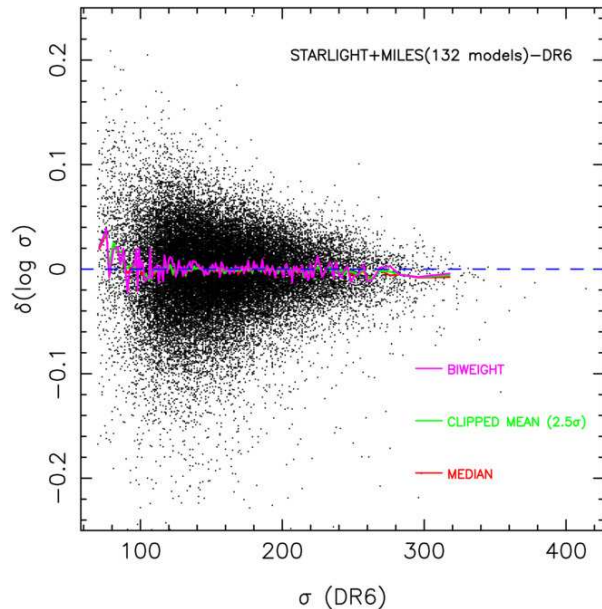
---

[7] Notice that the Sersic "n" is also correlated with velocity dispersion (Graham 2002), but the correlation exhibits a large dispersion.
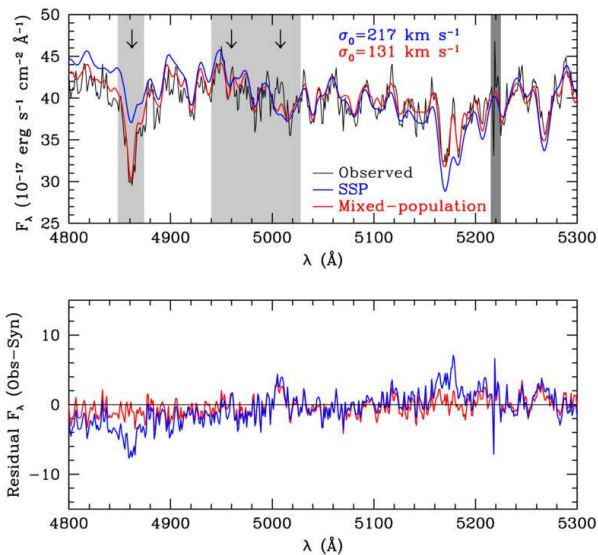
Figure 18. Example of the advantage in using mixed-population templates to derive the galaxy central velocity dispersion. The upper panel shows an example ETG spectrum from SDSS (J154615.45-001025.4) and the best-matching synthetic models obtained by running STARLIGHT (i) with a set of 132 different SSP MILES models (red color), and (ii) with a single SSP model, having an age of 12.6 Gyr and solar metallicity (blue color). The σ_0 values obtained in the two cases are reported in the upper panel. The lower panel shows the residuals obtained by subtracting the models to the observed spectrum. The gray bands in the upper panel show the masked windows we use to exclude from the fitting those regions possibly contaminated by emission lines (see the arrows in the plot) as well as corrupted pixels (e.g. those corresponding to bad-columns).


Figure 19. Differences in $\log \sigma_0$ between STARLIGHT and SDSS as a function of the SDSS velocity dispersion value. Curves with different colors are obtained by binning the data with respect to σ_0(DR6), and taking for each bin the corresponding median value (red), the location value estimated through the the bi-weight statistics (magenta), and the 2.5σ clipped mean value (green). Notice that the trend with σ is essentially the same for all the three estimators. The horizontal blue dashed line marks the value of zero, corresponding to a null difference between SDSS and STARLIGHT σ_0 values.

total of 132 SSP models. Fig. 18 illustrates the advantage of using a mixed-population rather than a single stellar population template. In order to exacerbates the difference between the two approaches, we selected the spectrum of one ETG for which STARLIGHT measures a significant contribution from young (age< 2 Gyr) stellar populations. The Figure plots a portion of the spectrum, along with two best-fitting models obtained by either the mixed-population approach (in red) or by running STARLIGHT with a single old stellar population template having an age of 12.6 Gyr and solar metallicity (in blue). Residuals are plotted for both cases. It is evident that the mixed-population model yields a better description of the continuum and the absorption features in the galaxy spectrum. In particular, one may notice that the Mgb band ($\lambda \sim 5170$Å), which is one of the main spectral features to measure the σ_0, shows significantly smaller residuals in the case of the mixed-population fit. In fact, the σ_0 value (reported in the upper panel of Fig. 18) changes dramatically from one case to the other. Fig. 18 also shows the masked regions used to avoid either corrupted spectral regions (e.g., bad columns) or regions possibly contaminated by nebular emission. In particular, we show three masked regions. The ones at $\lambda \sim 4850$ and 4980 Å avoid the Hβ (4861Å) and [OIII] (4959 and 5007) emission lines, respectively, while the one at $\sim$5220 Å excludes pixels contaminated by a bad-column, as flagged in the SDSS spectrum.

Fig. 19 compares velocity dispersion values obtained from the SDSS spectroscopic pipeline with those measured in this work using STARLIGHT. A good agreement is found, with only a small systematic trend at the low (< 90km/s) and high (> 280km/s) ends

of the σ_0 range. In particular, for $\sigma_0 < 90$km/s, the STARLIGHT velocity dispersions are slightly higher, by a few percent, with respect to those of the SDSS. It is important to emphasize that although STARLIGHT does not normalize the spectrum by the continuum, which is done by the direct fitting method used in the SDSS pipeline, the good agreement found here is likely reflecting the excellent quality of flux calibration obtained in DR6 (see Figure 7 of Adelman-McCarthy et al. 2008).The impact of the above systematic difference in σ_0 on the scaling relations of ETGs is investigated in paper II.

7.2 Uncertainties on the velocity dispersions

To estimate the uncertainties on the STARLIGHT σ_0 values, we looked for ETGs in the SPIDER sample having spectra with repeated observations in SDSS. Out of all the 39,993 galaxies, we found 2,313 cases with a duplicate spectrum available. For all these duplicate spectra, we measure the σ_0 with STARLIGHT, with the same setup and set of model templates as for the primary spectra. In each case, we compute the relative difference of σ_0 as $\delta\sigma/\sigma = (\sigma_{0,2} - \sigma_{0,1})/\sigma_{0,1}$, where the indices 1 and 2 refer to the spectra with higher and lower S/N ratios. Fig. 20 plots the $\delta\sigma/\sigma$ as a function of the minimum S/N ratio, $min(S/N)$, of each pair of duplicate spectra. The S/N is computed from the median S/N ratio in the spectral region of the H$_\beta$ feature, within a window of 100Å, centered at $\lambda = 4860$Å. We bin the $\delta\sigma/\sigma$ values with respect to $min(S/N)$, with each bin including 30 galaxies. For each bin, we compute the median and rms values of $\delta\sigma/\sigma$. As the Fig. 20 shows, the median values (red color) are fully consistent with zero, implying that, as expected (see Sec. 2), the S/N ratio of the spectra is large
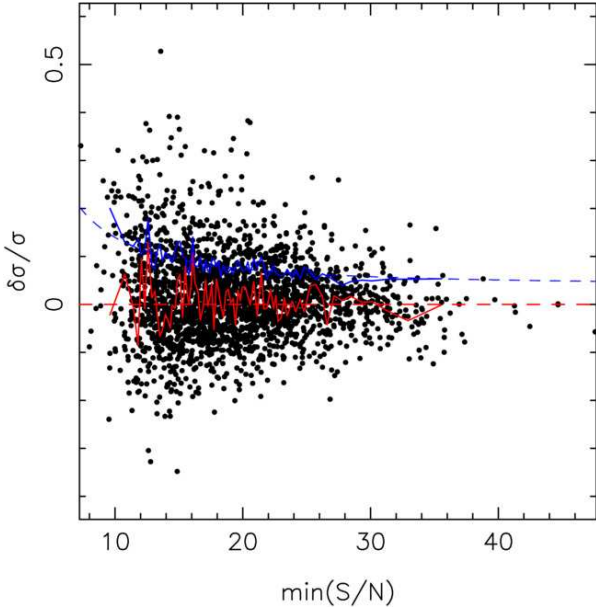
Figure 20. Relative differences of σ_0 values, $\delta\sigma/\sigma$, for ETG's spectra with repeated measurements available from SDSS. Each relative difference is computed with respect to the value obtained for the spectrum with highest S/N ratio. On the x-axis, the minimum S/N ratio, $min(S/N)$, of each pair of spectra is plotted. The red solid curve shows the median difference values obtained by binning the $\delta\sigma/\sigma$'s with respect to $min(S/N)$, with each bin including the same number of 30 galaxies. The red dashed curve marks the value of zero in the plot. The blue solid curve shows rms of difference's values in each bin. The dashed blue line is obtained by modeling the rms values by Eq. 6.

enough to obtain unbiased velocity dispersion estimates. The rms values, rms_{σ_0}, provide an estimate of the error on STARLIGHT σ_0 values. The rms_{σ_0} increases at low S/N ratio and is well described, as shown in Fig. 20, by the following functional form:

$$rms_{\sigma_0} = 0.0383 + 3.2 \times min(S/N)^{-1.5}. \qquad (6)$$

For each galaxy in the SPIDER sample, we assign the error on the STARLIGHT σ_0 value using the above equation, replacing $min(S/N)$ with the median S/N ratio in the H_β region (see above) of the corresponding galaxy spectrum. Notice that this procedure assumes that the error on σ_0 depends only on the S/N ratio, and is the same, for a given S/N, for both low and high σ_0 galaxies. In fact, we verified that considering only galaxies with $\sigma_0 < 130 \, km \, s^{-1}$, the dashed blue curve in Fig. 20 does not change significantly, shifting upwards by less than 2%. Fig. 21 compares the distribution of uncertainties of the SDSS and STARLIGHT σ_0 values. The STARLIGHT distribution is significantly narrower than that of SDSS. This is likely due to the fact that we are using a one parameter (i.e. the S/N ratio) function to assign the errors (see Eq. 6). However, the peak position of both distributions is very similar. In fact, the median values of SDSS errors and STARLIGHT rms_{σ_0}'s are fully consistent, amounting to ~ 0.07dex ($\sim 15\%$).

8   COMPLETENESS

8.1   SDSS vs. 2DPHOT completeness in r band

We first analyze the completeness of the SPIDER sample in r band. The completeness of SDSS data is well characterized with respect
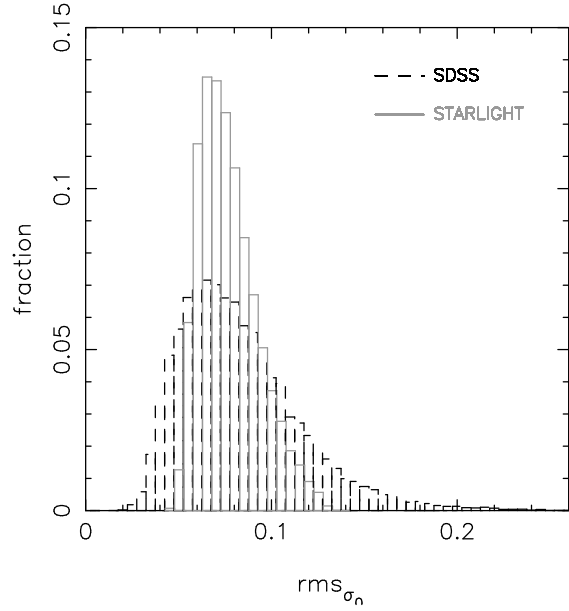
Figure 21. Distribution of uncertainties on SDSS (dashed-black) and STARLIGHT (gray) σ_0 values. A small offset of $+0.004$ has been applied to the gray histogram to make the plot more clear.

to the Petrosian magnitude, $m_{p,r}$, which is one of the main selection criteria used to target objects for SDSS spectroscopy. Here, we adopt $m_{p,r} = 17.77$ as the reference value for the spectroscopic completeness (Strauss et al. 2002). On the other hand, effective parameters are defined in terms of either the model magnitudes (SDSS) or Sersic total magnitudes (2DPHOT). As shown in Blanton et al. (2001), the difference between Petrosian and model magnitudes depends on galaxy half-light radii. Moreover, as discussed in Sec. 6, there are large systematic differences between *Photo* model magnitudes, m_{dev}, and the 2DPHOT Sersic total magnitudes, m_T. This implies that the m_p limit maps into a different completeness magnitude value when using either SDSS or 2DPHOT parameters. In the following, we denote the absolute m_{dev} magnitude as $^{0.07}M_{dev,r}$, and total 2DPHOT magnitudes as $^{0.07}M_r$, characterizing the completeness of the SPIDER sample with respect to both $^{0.07}M_{dev,r}$ and $^{0.07}M_r$. We also use the symbol M_r to refer indistinctly to either one or the other total magnitude. Fig. 22 plots SDSS and 2DPHOT absolute magnitudes as a function of $m_{p,r}$. At a given $m_{p,r}$, the scatter seen in the plot reflects all the different factors that enter the definition of total absolute magnitudes, i.e. the k- and galactic extinction corrections, the redshift range of the sample, as well as the intrinsic difference between M_r and m_p (see above). Assuming the SDSS sample to be complete down to $m_{p,r} = 17.77$, we define here 95% completeness limits for $^{0.07}M_{dev,r}$ and $^{0.07}M_r$, by adopting the geometric approach illustrated in the figure. The method is similar to that described by Garilli, Maccagni, & Andreon (1999), where the completeness limit of a galaxy sample is defined as that magnitude where galaxies begin to be missed in it because of the surface brightness detection limit. In practice, we select a range in absolute magnitude where all galaxies have $m_{p,r}$ smaller than the SDSS spectroscopic completeness limit of 17.77. We consider the ranges of -20.7 to -21.7 and -21 to -22 for $^{0.07}M_{dev,r}$ and $^{0.07}M_r$, respectively. Then, in these ranges, we bin the distribution of $m_{p,r}$ values with respect to M_r, and derive the 95% percentile of the $m_{p,r}$ distribution in each bin. The binned points are fitted with
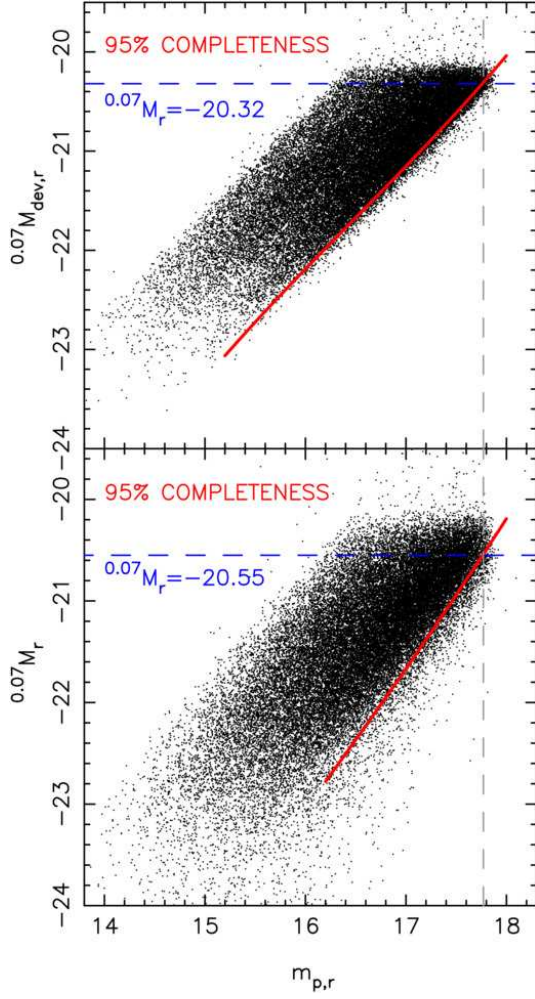
Figure 22. Completeness limits of the ETG sample for the SDSS absolute model magnitudes (upper-panel) and 2DPHOT absolute Sersic magnitudes (lower-panel) in r-band. The vertical dashed gray line in each panel marks the Petrosian magnitude limit, $m_{p,r} = 17.77$, of the SDSS spectroscopy. The red curve is obtained by a second polynomial fit of the 95% percentile values of the $m_{p,r}$ distributions in different bins of total magnitude (see the text). The horizontal dashed lines mark the points where the red curves cross the vertical line, defining the 95% completeness limits of the sample.

a second order polynomial, shown by the red curves in Fig. 22. The M_r value where the polynomial intersects the vertical line of $m_{p,r} = 17.77$ defines the point below which at least 95% of the galaxies, for whatever value of M_r, are included in the sample. We refer to the value of M_r at the intersection point as the 95% completeness limit of the sample. Notice that the 2DPHOT completeness limit is brighter than that of the model magnitudes. The difference, ~ 0.2mag, matches the average difference between $^{0.07}M_{dev,r}$ and $^{0.07}M_r$ measured for the faintest galaxies in the SPIDER sample (see Sec. 6).

8.2 Completeness from g through K

We apply the geometric approach of Sec. 8.1 to characterize the completeness limit of the SPIDER sample in all wavebands. Since our main goal is that of selecting volume limited samples for analyzing the FP relation in each waveband (papers II and III), we

Table 3. Completeness limits in $grizYJHK$. Column 1: waveband. Column 2: 95% completeness magnitude. Column 3: number of galaxies brighter than the completeness limit.

| waveband	$^{0.07}M_X$ limit	N
g	-19.71	35989
r	-20.55	36205
i	-20.98	35711
z	-21.22	36310
Y	-21.95	4652
J	-22.54	6432
H	-23.21	5823
K	-23.62	5690

consider here only 2DPHOT Sersic magnitudes, which are linearly related to $\log r_e$ and $< \mu >_e$, and hence are the relevant quantities to characterize the completeness of the sample in the space of effective parameters. Fig. 23 plots the total Sersic magnitudes, $^{0.07}M_X$, as a function of $m_{p,r}$, where X is one of the available wavebands (i.e. $X = grizYJHK$). For a given band, we define an absolute magnitude range of $^{0.07}M_{X_1}$ to $^{0.07}M_{X_2}$, where the sample is complete with respect to $m_{p,r}$, and bin the corresponding distribution of $m_{p,r}$ values with respect to the $^{0.07}M_X$. The 95% completeness magnitude in the band X is then defined as described in Sec. 8.1. For each band, the values of $^{0.07}M_{X_1}$ and $^{0.07}M_{X_2}$ are obtained by trasforming those in r-band through the median values of the ETG's color indices (see Tab. 2). For each band, the 95% completeness limit is reported in Tab. 3, together with the number of SPIDER ETGs brighter than that limit.

9 SUMMARY

The data presented in this paper represents the most extensive ever obtained for early-type galaxies. Optical data from SDSS were entirely reprocessed; images with 2DPHOT (La Barbera et al. 2008) and spectra with STARLIGHT, as described above. This allows us to perform a proper comparison of different pipelines. We have created a database to store all of the photometric and spectroscopic parameters measured as part of our reprocessing. The SPIDER database (SdB) currently contains only the photometric (SDSS and UKIDSS) and spectroscopic (SDSS) data described here, but we expect to incorporate additional data from other wavelength regimes. The SdB architecture is extensible and designed to support this growing process. We are currently developing an intuitive Graphic User Interface (GUI) which will allow the user to easily retrieve all information available in the SdB issuing SQL queries. Until the GUI is ready for general use we are making the data available through the link

http://www.lac.inpe.br/bravo/arquivos/SPIDER_data_paperI.ascii.[8]

The data presented here will be used in the forthcoming papers analyzing the FP relations (papers II and III). Given the importance of obtaining meaningful measurements of the structural parameters entering the FP, this contribution examines how consistent these parameters are and their errors. Here we summarize the main properties of the sample defined in this paper and the characteristic parameters of each ETG:

---

[8] A mirror is also available at http://www.na.astro.it/ labarber/SPIDER/.

[!ht]
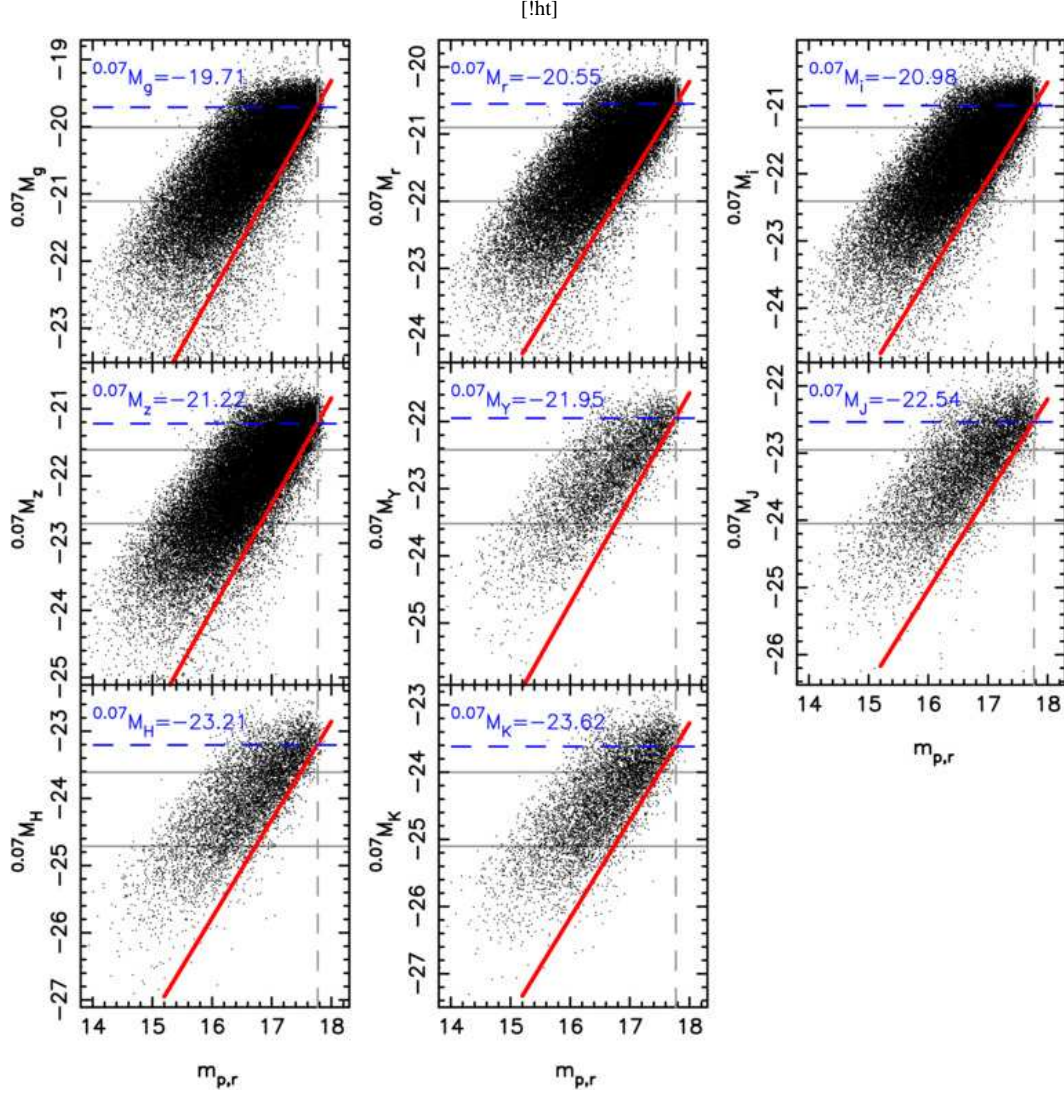
Figure 23. Completeness limits in the $grizYJHK$ bands. Each panel is the same as the lower panel in Fig. 22, but for a different waveband, X. The X runs from g to K going from left to right, and top to bottom in the figure. The upper–mid panel is the same as the lower panel of Fig. 22, and is repeated here for a better comparison among all the wavebands. The 95% completeness limits (see the text) are reported in the upper–left corners of the panels. The two solid gray horizontal lines indicate the absolute magnitude range of $^{0.07}M_{X_1}$ to $^{0.07}M_{X_2}$, where the sample is complete with respect to $m_{p,r}$,

1 - When matching optical+NIR data we end-up with 5,080 ETGs which can then be used to study the global properties of elliptical galaxies in the nearby Universe (z<0.1).

2 - For each of these ETGs we have measured aperture and total magnitudes, k-corrected and dereddened for galactic extinction. We also quantify for each galaxy the following essential parameters: effective (half-light) radius, r_e, the mean surface brightness within this radius, $<\mu>_e$, the Sersic index (shape parameter) n, the axis ratio b/a, and the position angle of the major axis, PA. Besides, the galaxy isophotal shape is characterized by the a_4 parameter.

3 - Uncertainties in all of the parameters previously listed are estimated and presented as a function of the logarithm of the signal-to-noise per pixel. Median errors in r_e, $<\mu>_e$, and n are ~ 0.1, $\sim 0.5\ mag/arcsec^2$, and ~ 0.1, respectively, in the optical, and ~ 0.15, $\sim 0.6\ mag/arcsec^2$, and ~ 0.12 in the NIR.

4 - We do not find any systematic steepening of the CM relation when considering a waveband baseline from $g-r$ to $g-K$,

as expected if the *total* CM relation is solely driven by a mass–metallicity relation in ETGs. According to Scodeggio (2001), this result can be interpreted as follows: ETGs have negative color gradients, with color indices becoming bluer from the galaxy center to its outskirts. Thus, when we adopt colors in a fixed aperture, we measure a color inside a smaller region (with respect to r_e) for the brightest (hence larger) galaxies than for faintest galaxies in the sample, leading to a misleading steepening of the CM relation

5 - The study presented here of the structural parameters of ETGs reveals the following properties: log r_e decreases by 35% from the optical to the NIR, reflecting the internal color gradients in these systems; the axis ratios, b/a, have their distribution essentially constant from g through K, with a media value of ~ 0.7 and width of ~ 0.2; The Sersic index is always larger than 1, since we selected only bulge dominated galaxies and spans a domain from ~ 2 to ~ 10, with a median of 6 for all wavebands; no systematic trend of a_4 was found from g to i.

6 - We present measurements of central velocity dispersion

obtained using STARLIGHT. Extensive comparison with the estimates provided by the SDSS pipeline, shows that our estimates are unbiased over the whole $\sigma_\circ$ range, with a median error of $\sim15\%$.

7 - Comparison of two independent pipelines was done (SDSS and 2DPHOT) and reveals significant differences in magnitude and effective radius with respect to the Sersic index and absolute model magnitude in r-band. The impact of such differences on the scaling relations of ETGs will be addressed in paper II.

REFERENCES

Abazajian, K.N., Adelman-McCarthy, J.K., Agüeros, M.A., et al., 2009, ApJS, 182, 543

Adelman-McCarthy, J.K., Agüeros, M.A., Allam, S.S., et al., 2008, ApJS, 175, 297

Beers, T.C., Flynn, K., Gebhardt, K., 1990, AJ, 100, 32

Bender, R., Möllenhoff, C., 1987, A&A, 177, 71 (BM87)

Bernardi, M., Sheth, R.K., Annis, J., 2003a, AJ, 125, 1849

Bernardi, M., Sheth, R.K., Annis, J., 2003b, AJ, 125, 1866

Bernardi, M., Nichol, R.C., Sheth, R.K., Miller, C.J., Brinkmann, J., 2006, AJ, 131, 1288

Bernardi, M., Hyde, J.B., Sheth, R.K., Miller, C.J., Nichol, R.C., 2007, AJ, 133, 1741

Bertin, E., Arnout, S., 1996, A&AS, 117, 393

Blanton, M.R., Dalcanton, J., Eisenstein, D., 2001, AJ, 121, 2358

Blanton, M.R., Lin, H., Lupton, R.H., Maley, F.M., Young, N., Zehavi, I., Loveday, J., 2003, AJ, 125, 2276 (BL03)

Blanton, M.R., Hogg, D.W., Bahcall, N.A., 2003, ApJ, 594, 186

Bonifacio, P., Monai, S., Beers, T.C., 2000, AJ, 120, 2065

Brosche, P., 1973, A&A, 23, 268

Bruzual, G., & Charlot, S. 2003, MNRAS, 344, 1000 (BrC03)

Bujarrabal, V., Guibert, J., Balkowski, C., 1981, A&A, 104, 1

Caon, N., Capaccioli, M., & D'Onofrio, M., 1993, MNRAS, 265, 1013

Capaccioli, M., Caon, N., & D'Onofrio, M. 1992, MNRAS, 259, 323

Casali, M., Adamson, A., Alves de Oliveira, C., et al., 2007, A&A, 467, 777

Cid Fernandes, R., González Delgado, R.M., Storchi-Bergmann, T., Martins, L.P., Schmitt, H., 2005, MNRAS, 356, 270

Djorgovski, S.G., & Davis, M., 1987, ApJ, 313, 59

D'Onofrio, M., Fasano, G., Varela, J., et al., 2008, ApJ, 685, 875

Dressler, A., Lynden-Bell, D., Burstein, D., Davies, R.L., Faber, S.M., Terlevich, R., Wegner, G., 1987, ApJ, 313, 42

Efstathiou, G., Fall, S.M., 1984, MNRAS, 206, 453

Gargiulo, A., Haines, C.P., Merluzzi, P., Smith, R.J., et al., 2009, MNRAS, 397, 75

Garilli, B., Maccagni, D., & Andreon, S., 1999, A&A, 342, 408

Gómez, P.L., Nichol, R.C., Miller, C.J., et al., 2003, ApJ, 584, 210

Graham, A.W., 2002, MNRAS, 334, 859

Graham, A., Colless, M., 1997, MNRAS, 287, 221

Graham, A. W., Guzmán, R., 2003, AJ, 125, 2936

Graham, A.W., Driver, S.P., Petrosian, V., Conselice, C.J., Bershady, M.A., Crawford, S.M., Goto, T., 2005, AJ, 130, 1535

Hambly, N.C., Collins, R.S., Cross, N.J.G., et al. 2008, MNRAS, 384, 637

Hewett, P.C., Warren, S.J., Leggett, S.K., Hodgkin, S.T., 2006, MNRAS, 367, 454

Hodgkin, S.T., Irwin, M.J., Hewett, P.C., Warren, S.J., 2009, MNRAS, 394, 675

Hogg, D.W., Blanton, M.R., Brinchmann, J., et al., 2004, ApJ, 601, 29

Hyde, J.B., Bernardi, M., 2009, MNRAS, 394, 1978

Jørgensen, I., Franx, M., Kjærgaard, P., 1996, MNRAS, 280, 167

Ko, J., Im, M., 2005, J. Korean Astron. Soc., 38, 149

Kron, R.G., 1980, ApJS, 43, 305

La Barbera, F., de Carvalho, R.R., Kohl-Moreira, J.L., Gal, R.R., Soares-Santos, M., Capaccioli, M., Santos, R., Sant'anna, N., 2008, PASP, 120, 681 (LdC08)

La Barbera, F., Busarello, G., Merluzzi, P., de la Rosa, I.G., Coppola, G., Haines, C.P., 2008, ApJ, 689, 913

La Barbera, F., de Carvalho, R.R., 2009, ApJL, 699, 76

Lauer, T.R., Faber, S.M., Richstone, D., et al., 2007, ApJ, 662, 808

Lawrence, A., Warren, S.J., Almaini, O., et al. 2007, MNRAS, 379, 1599

Maller, A.H., Berlind, A.A., Blanton, M.R., Hogg, D.W., 2009, ApJ, 691, 394

Okamura, S., Kodaira, K., Watanabe, M., 1984, ApJ, 280, 70

Pahre, M.A., 1999, ApJS, 124, 127

Peletier, R.F., Valentijn, E.A., Jameson, R.F., 1990, A&A, 233, 62

Prugniel, P., Simien, F., 1996, A&A, 309, 749

Saglia, R.P., Colless, M., Burstein, D., Davies, R.L., McMahan, R.K., Wegner, G., 2001, MNRAS, 324, 389

Sánchez-Blázquez, P., Peletier, R. F., Jiménez-Vicente, J., et al., 2006, MNRAS, 371, 703

Schlegel, D., Finkbeiner, D.P., Davis, M., 1998, ApJ, 500, 525

Scodeggio, M., 2001, AJ, 121, 2413

Shimasaku, K., Fukugita, M., Doi, M., et al., 2001, AJ, 122, 1238

Sorrentino, G., Antonuccio-Delogu, V., Rifatto, A., 2006, A&A, 460, 673

Sparks, W.B., & Jörgensen, I., 1993, AJ, 105, 5

Spolaor, M., Proctor, R.N., Forbes, D.A., Couch, W.J., 2009, ApJ, 691, 138

Stoughton, C., Lupton, R.H., Bernardi, M., et al., 2002, AJ, 123, 485

Strauss, M.A., Weinberg, D.H., Lupton, R.H., et al., 2002, AJ, 124, 1810

Strateva, I., Ivezić, Z., Knapp, G.R., et al., 2001, AJ, 122, 1861

Vazdekis, A., Sanchez-Blazquez, P., Falcon-Barroso, J., Cenarro, A.J., Beasley, M.A., Cardiel, N., Gorgas, J., Peletier, R.F., 2010, MNRAS, in press

Warren, S.J., Hambly, N.C., Dye, S., et al., 2007, MNRAS, 375, 213

Weinmann, S.M., Kauffmann, G., van den Bosch, F.C., Pasquali, A., McIntosh, D.H., Mo, H., Yang, X., Guo, Y., 2009, MNRAS, 394, 1213

Whitmore, B.C., 1984, ApJ, 278, 61

This paper has been typeset from a TEX/ LATEX file prepared by the author.